Supporting Information for Accurate ^{19}F NMR Chemical Shifts in Fe(II) Complexes with the LH20t Local Hybrid Functional

Justin Krampe, Timon Zankel, Roman Kornievskii, Kilian Heckenberger, Vera Krewald,* and Christina M. Thiele*

E-mail: vera.krewald@tu-darmstadt.de; cthiele@thielelab.de

Contents

1 Overview of the Fe complexes **S2**

2 Spin State Energies **S3**

3 Prediction accuracy of ^{1}H & ^{13}C spectra **S4**

4 Solvent Dependence of Reference Chemical Shifts **S12**

5 Experimental NMR, IR & UV/Vis-Spectra **S14**
5.1 NMR sample preparation S14
5.2 Complex **2** - $[Fe(bpy-4,4'-F)_3]^{2+}$ S16
5.3 Complex **3** - $[Fe(bpy-4,4'-CF_3)_3]^{2+}$ S20
5.4 Complex **5** - $[Fe(tpy-ph-4\text{-}F)_2]^{2+}$ S24
5.5 Complex **8** - $[Fe(tpp-F_{20})]$ S27
5.6 Complex **9** - $[Fe(pc-F_{16})]$ S29
5.7 Complex **10** - $[Fe(phen-(ph-3,5-(CF_3)))_3]^{2+}$ S33

6 CREST **S38**

References **S39**

1 Overview of the Fe complexes

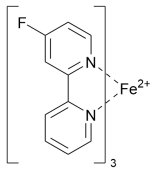

1 $[Fe(bpy\text{-}4\text{-}F)_3]^{2+}$

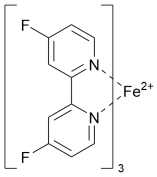

2 $[Fe(bpy\text{-}4,4'\text{-}F)_3]^{2+}$

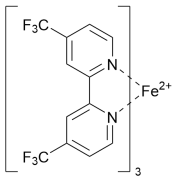

3 $[Fe(bpy\text{-}4,4'\text{-}CF_3)_3]^{2+}$

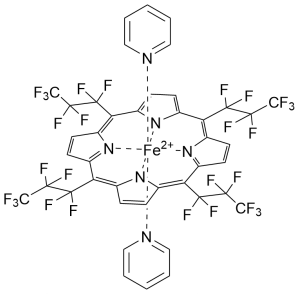

4 $[Fe(py)_2(por\text{-}(C_3F_7)_4)]$

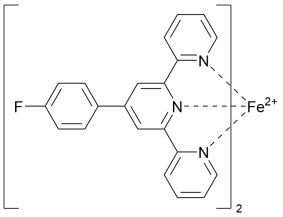

5 $[Fe(tpy\text{-}ph\text{-}4\text{-}F)_2]^{2+}$

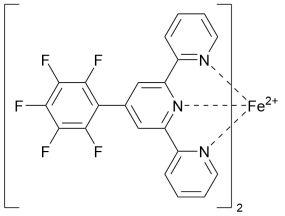

6 $[Fe(tpy\text{-}ph\text{-}F_5)_2]^{2+}$

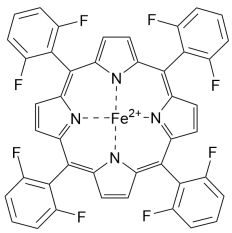

7 $[Fe(tpp\text{-}F_8)]$

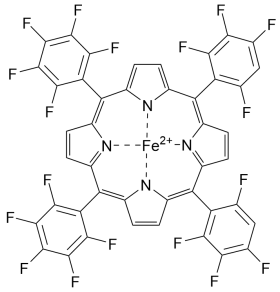

8 $[Fe(tpp\text{-}F_{20}]$

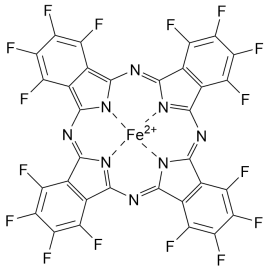

9 $[Fe(pc\text{-}F_{16})]$

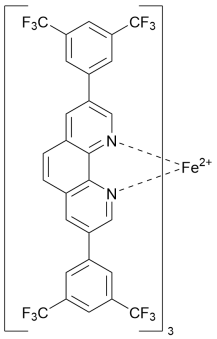

10 $[Fe(phen\text{-}(ph\text{-}3,5\text{-}(CF_3))_2)_3]^{2+}$

Figure S1: Iron complexes included in the benchmarking set.

2 Spin State Energies

Table S1: Spin state energies in kcal/mol of all ten complexes including the *fac* and *mer* isomers of $[Fe(bpy-4\text{-}F)_3]^{2+}$ calculated using the OPBE functional, the CP(PPP) basis set for iron and the def2-TZVP basis set for the remaining atoms.

		Single-Point Calculation		
Nr.	Complex	M=1	M=3	M=5
1	*fac* $[Fe(bpy-4\text{-}F)_3]^{2+}$	0.00	36.42	57.03
1	*mer* $[Fe(bpy-4\text{-}F)_3]^{2+}$	0.02	36.12	56.74
2	$[Fe(bpy-4,4'-F)_3]^{2+}$	0.00	35.08	53.67
3	$[Fe(bpy-4,4'-CF_3)_3]^{2+}$	0.00	36.09	58.35
4	$[Fe(py)_2(por-(C_3F_7)_4)]$	0.00	20.58	44.68
5	$[Fe(tpy-ph-4\text{-}F)_2]^{2+}$	0.00	37.81	66.07
6	$[Fe(tpy-ph-F_5)_2]^{2+}$	0.00	37.54	66.26
7	$[Fe(tpp-F_8)]$	36.98	0.00	26.49
8	$[Fe(tpp-F_{20})]$	36.81	0.00	11.84
9	$[Fe(pc-F_{16})]$	14.90	0.00	27.94
10	$[Fe(phen-(ph-3,5-(CF_3))_2)_3]^{2+}$	0.00	35.44	50.18

In addition to the geometry optimisations for the complexes **2**-**10** and the *fac* and *mer* isomers of $[Fe(bpy-4\text{-}F)_3]^{2+}$ **1**, we also performed single-point energy calculations for the singlet, triplet, and quintet states of all complexes using an internally benchmarked level of theory, which are summarised in Table S1. As already noted in the main text, complexes **1**-**6** and complex **10** exhibit a clear singlet ground state, whereas the two tetraphenylporphyrin complexes (**7** and **8**) and the phthalocyanine (**9**) each display a clear triplet ground state. All other spin states lie more than 10 kcal/mol higher in energy and are therefore not thermally populated at room temperature.

To assess whether the predicted relative energies are consistent with the experimentally observed *fac* : *mer* ratio of approximately 3 : 1 for the $[Fe(bpy-4\text{-}F)_3]^{2+}$ complex (**1**), we compared the spin-state energies of both isomers relative to the singlet energy of the *fac*-isomer singlet ground state. As shown in Table S1, the singlet ground-state geometries of the two isomers are isoenergetic (energy difference of only ca. 0.02 kcal/mol). This indicates that both isomers are thermodynamically accessible at room temperature. A simple

Boltzmann analysis yields an equilibrium composition of roughly 50.8% *fac* and 49.2% *mer*. However, this number should not be overinterpreted, as the exact ratio is strongly affected by the predicted energy difference, which is in turn affected by the choice of functional, the inclusion of explicit solvent molecules, and the treatment of dispersion. Therefore, our single-point analysis only establishes that both stereoisomers are thermally accessible, but does not predict the experimentally determined *fac* : *mer* ratio in solution.

3 Prediction accuracy of ^{1}H & ^{13}C spectra

We additionally analyzed the ^{1}H shifts for complexes **1**–**6**, **8**, and **10**, as well as the ^{13}C shifts for complexes **2**, **3**, **5**, **9**, and **10**, where experimental data were available. These calculations were used to assess whether the superior predictive performance of LH20t observed for ^{19}F also extends to ^{1}H and ^{13}C. However, a clear conclusion could not be drawn, owing to the limited data set and the comparatively narrow spectral dispersion of ^{1}H and ^{13}C signals.

For ^{1}H NMR, the aromatic region between 7 and 9 ppm contained more than 32 protons, whereas only three protons were present in the aliphatic region. For ^{13}C NMR, the 37 measured carbon signals spanned a range of roughly 50 ppm but originated from only five complexes, limiting statistical robustness. Moreover, both datasets contained only one complex with a triplet-state geometry, preventing any clear conclusions about paramagnetic contributions to these shifts. Overall, the current data are insufficient for a reliable interpretation, and further studies with a larger and more balanced dataset are needed.

The best protocol for predicting ^{1}H data in Figure S2 shows mean absolute deviations comparable to the $\approx$ 0.15 ppm reported by de Olivera *et al.*[1] The best performance for the ^{1}H set was obtained with TPSSh, which includes 10% Fock exchange, yielding a MAD of 0.40 ppm for pcSseg-2. B3LYP, PBE0, and LH20t produced MADs in the range of 0.48–0.57 ppm for the same basis set. The improvement observed for LH20t in the ^{19}F analysis therefore cannot be directly generalised to other nuclei. Other local hybrid and range-separated local

hybrid functionals have to be tested for their predictive performance on ^{1}H shifts.

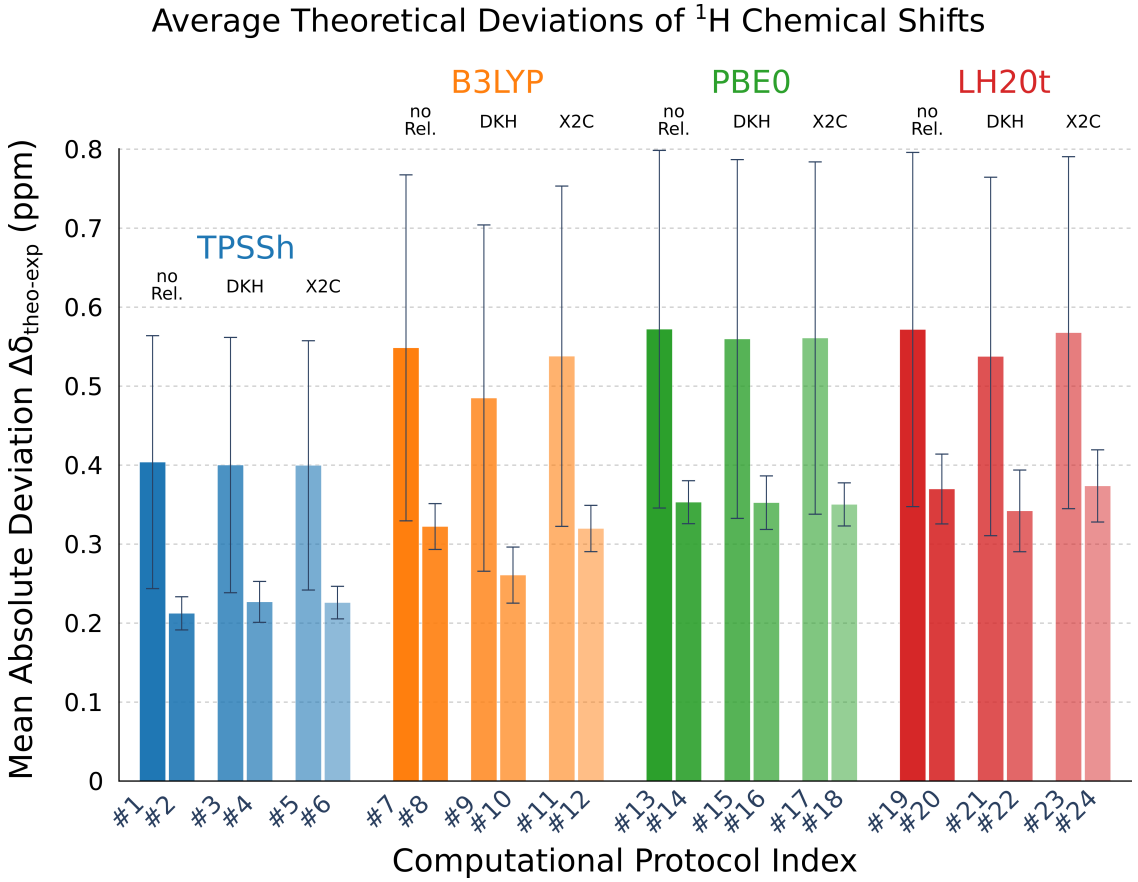

Figure S2: Mean absolute deviations between calculated and experimental ^{1}H chemical shifts for all computational protocols listed in Table 1 of the main text, comparing the performance of global hybrid functionals (TPSSh, B3LYP, PBE0) and the local hybrid LH20t, using DKH, X2C, or no scalar relativistic correction (no Rel.). All odd-numbered protocols employ the pcSseg-2 basis set, while all even-numbered protocols use the pcSseg-3 basis set. The average standard deviations of all 35 individual hydrogen signals contained in this series are given as error bars.

Figure S2 additionally contains the average standard deviations of all unique groups of ^{1}H signals. For pcSseg-2, these standard deviations lie between 0.40–0.57 ppm, while for pcSseg-3 they range from 0.21–0.37 ppm across all tested functionals. The apparent improvement with the larger basis set must be interpreted cautiously: as noted in the main text, the computation with the pcSseg-3 set does not include the five hydrogens from the $[Fe(phen-(ph-3,5-(CF_3))_2)_3]^{2+}$ complex (**10**) with flexible ligands, which also show the largest MAD and standard deviation in the pcSseg-2 calculations. Excluding these sig-

nals inevitably improves the statistical measures. This indicates that a significant part of the inaccuracy arises from conformational degrees of freedom, leading to large deviations for the same hydrogen atoms. To better capture such effects, a conformer-rotamer-ensemble approach such as CREST, combined with Boltzmann-weighted averaging of calculated chemical shifts, could be applied. Such methods have already been shown to significantly reduce MADs for small organic molecules.[2]

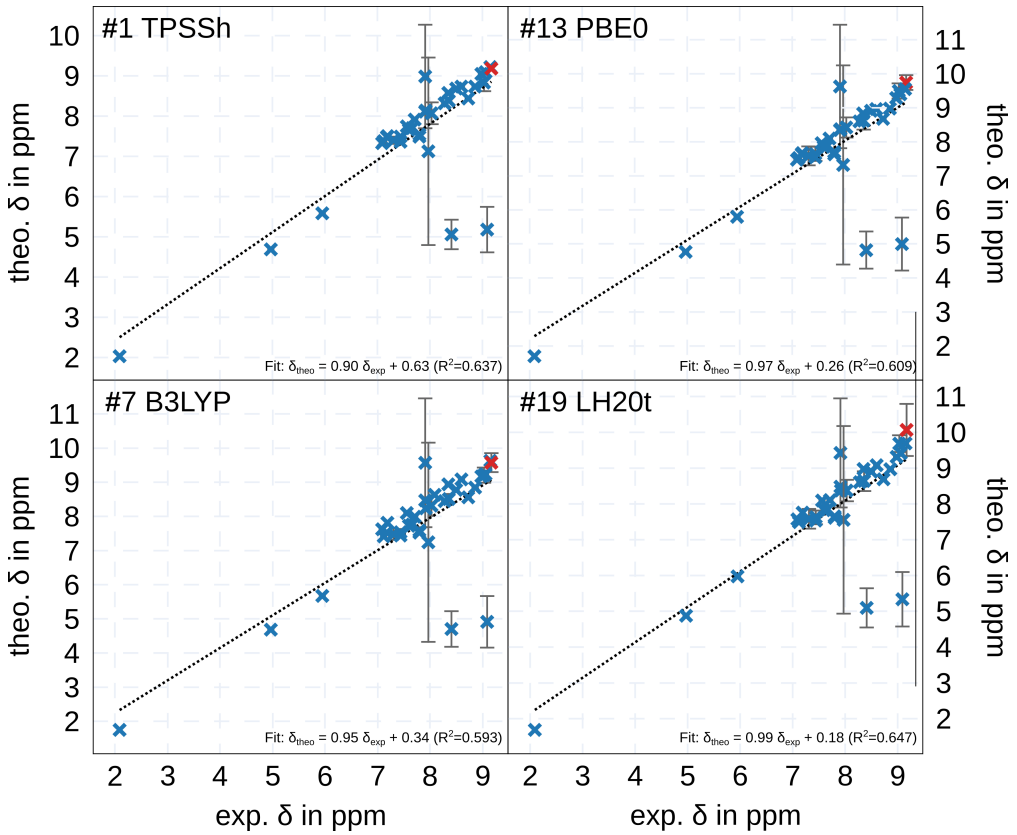

Figure S3: Correlation diagrams comparing theoretically calculated and experimentally measured ^{1}H chemical shifts, as summarised in Table S2. Blue crosses denote complexes with a singlet ground state (complexes **1-6** and **10**), while the red cross represents the single hydrogen in complex **8** (triplet ground state). Error bars indicate the standard deviation of the calculated shifts for each hydrogen site. The dashed line corresponds to the linear fitted theory–experiment correlation.

To more thoroughly analyse the predictive accuracy of all four functionals, Figure S3 presents correlation diagrams for pcSseg-2 without relativistic corrections. Unlike the main-text plots, here the black line represents the linear correlation between calculated and ex-

perimental values, thereby excluding uniform offsets across the series. This analysis shows that the prediction quality of ^{1}H shifts is comparable across all tested functionals, with no significant differences observed. All signals correlate reasonably well with experiment, except for three ^{1}H signals in the complex **10** at 7.91, 8.41, and 9.09 ppm, which as noted above show large deviations for all ^{1}H signals. The full set of calculated ^{1}H chemical shifts for all 35 protons is provided in Table S2.

Figure S4 summarises the mean absolute deviations (MADs) for the ^{13}C nuclei. Although ^{19}F and ^{13}C span similar chemical shift ranges of several hundred ppm, the predictive accuracy for ^{13}C is noticeably lower. The best-performing functional, as in the ^{1}H case, is TPSSh, with MADs between 7.4 and 7.6 ppm for pcSseg-2. This is closely followed by LH20t, with MADs of 9.2 to 9.3 ppm. The global hybrids B3LYP and PBE0 perform significantly worse, with MADs of 12.2 to 13.8 ppm.

Table S2: Summary of all 35 unique experimentally measured and theoretically calculated ^{1}H chemical shifts in the benchmarking set, obtained without relativistic corrections and using the pcSseg-2 basis set. Results correspond to computational protocols #1, #7, #13, and #19 as defined in Table 1 of the main text.

Nr.	Complex	Hydrogen	Exp.	TPSSh	B3LYP	PBE0	LH20t
1	$[Fe(bpy-4\text{-}F)_3]^{2+}$	H_3	8.73[a]	8.44	8.56	8.68	8.69
		H_5	7.44[a]	7.36	7.44	7.55	7.54
		H_6	7.80[a]	7.49	7.52	7.63	7.61
		$H_{3'}$	8.86[a]	8.73	8.84	8.98	8.97
		$H_{4'}$	8.28[a]	8.32	8.45	8.60	8.61
		$H_{5'}$	7.60[a]	7.66	7.72	7.85	7.83
		$H_{6'}$	7.80[a]	7.54	7.58	7.70	7.65
2	$[Fe(bpy-4,4'-F)_3]^{2+}$	H_3	8.37[b]	8.38	8.51	8.62	8.64
		H_5	7.32[b]	7.40	7.48	7.59	7.59
		H_6	7.45[b]	7.49	7.54	7.65	7.63
3	$[Fe(bpy-4,4'-CF_3)_3]^{2+}$	H_3	8.98[b]	9.05	9.17	9.29	9.31
		H_5	7.71[b]	7.91	7.99	8.10	8.11
		H_6	7.66[b]	7.70	7.76	7.87	7.84
4	$[Fe(py)_2(por-(C_3F_7)_4)]$	$H_{\beta'}$	9.03[c]	8.83	9.21	9.50	9.68
		$H_{py,\alpha}$	2.09[c]	2.03	1.75	1.70	1.69
		$H_{py,\beta}$	4.97[c]	4.69	4.68	4.77	4.88
		$H_{py,\gamma}$	5.95[c]	5.58	5.67	5.80	5.98
5	$[Fe(tpy-ph-4\text{-}F)_2]^{2+}$	H_1	7.19[b]	7.50	7.81	7.67	7.76
		H_2	7.09[b]	7.33	7.62	7.47	7.57
		H_3	7.91[b]	8.11	8.47	8.35	8.48
		H_4	8.60[b]	8.73	9.08	8.96	9.08
		H_5	9.15[b]	9.22	9.63	9.55	9.69
		H_6	8.35[b]	8.58	8.94	8.84	8.98
		H_7	7.56[b]	7.74	8.10	7.96	8.09
6	$[Fe(tpy-ph-F_5)_2]^{2+}$	H_1	7.18[d]	7.48	7.53	7.64	7.60
		H_2	7.12[d]	7.38	7.41	7.52	7.49
		H_3	7.92[d]	8.14	8.23	8.37	8.38
		H_4	8.50[d]	8.68	8.77	8.91	8.90
		H_5	9.06[d]	9.09	9.23	9.40	9.42
8	$[Fe(tpp-F_{20})]$	H	9.17[e]	9.18	9.57	9.74	10.07
10	$[Fe(phen-(ph-3,5-(CF_3))_2)_3]^{2+}$	H_1	8.41[b]	5.06	4.70	4.82	5.10
		H_2	9.09[b]	5.18	4.91	5.00	5.34
		H_3	7.97[b]	7.13	7.24	7.32	7.56
		H_4	7.91[b]	8.98	9.57	9.63	9.43
		H_5	8.03[b]	8.07	8.31	8.42	8.37

[a] $\delta_{ref}(CD_3CN) = 1.93$ ppm, solvent: $(CD_3)_2CO$, taken from Ref.[3] ; [b] internal Ref., solvent: CD_3CN, this work; [c] $\delta_{ref}(CHCl_3) = 7.24$ ppm, solvent: $CDCl_3$, taken from Ref.[4] ; [d] internal Ref., solvent: CD_3CN, taken from Ref.[5] ; [e] $\delta_{ref}(TMS) = 0.0$ ppm, solvent: toluene$-d_8$, taken from Ref.[6]

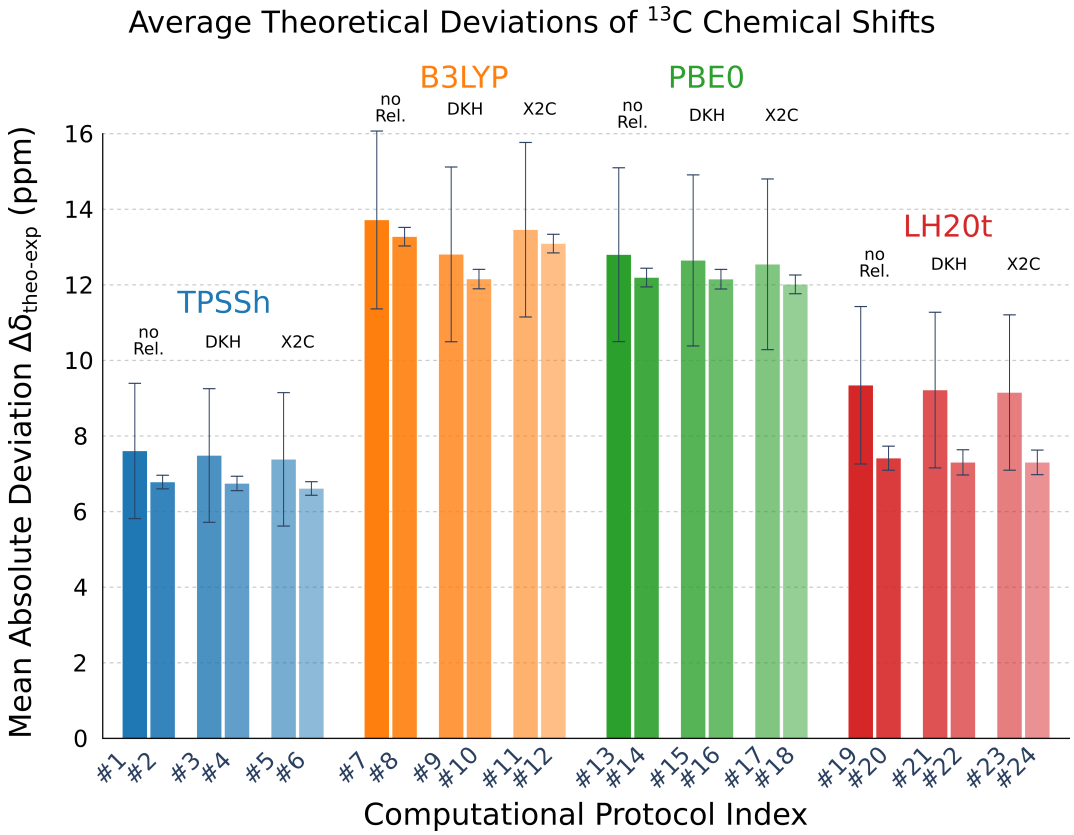

Figure S4: Mean absolute deviations between calculated and experimental ^{13}C chemical shifts for all computational protocols listed in the main text, comparing the performance of global hybrids (TPSSh, B3LYP, PBE0) and the local hybrid LH20t, using DKH, X2C, or no scalar relativistic correction (no Rel.). All odd-numbered protocols employ the pcSseg-2 basis set, while all even-numbered protocols use the pcSseg-3 basis set. The average standard deviations of all 37 individual carbon signals contained in this series are given as error bars.

An interesting difference emerges in the basis set dependence: for the global hybrids, switching from pcSseg-2 to pcSseg-3 improves accuracy by just over 1 ppm, whereas for LH20t the improvement reaches up to 1.9 ppm. This indicates a pronounced basis set sensitivity for LH20t in ^{13}C predictions, an effect not observed for ^{19}F or ^{1}H.

The same figure also shows average standard deviations of 1.7 to 2.3 ppm for pcSseg-2 and 0.2 to 0.3 ppm for pcSseg-3, across all functionals. However, the apparent improvement in standard deviation must be interpreted with caution: ten unique carbon signals from complex **10**, which exhibit the largest deviations, are absent from the pcSseg-3 dataset.

Correlation diagrams for the ^{13}C data (seen in Figure S5) were generated in the same way

as for ^{1}H, with the black line representing the linear fit between theoretical and experimental values. For the global hybrids, the theory–experiment correlation is generally excellent, with two main exceptions: The ten carbon signals of complex **10** with flexible ligands and the four signals in the paramagnetic complex **9**, where deviations increase with proximity to the paramagnetic center.

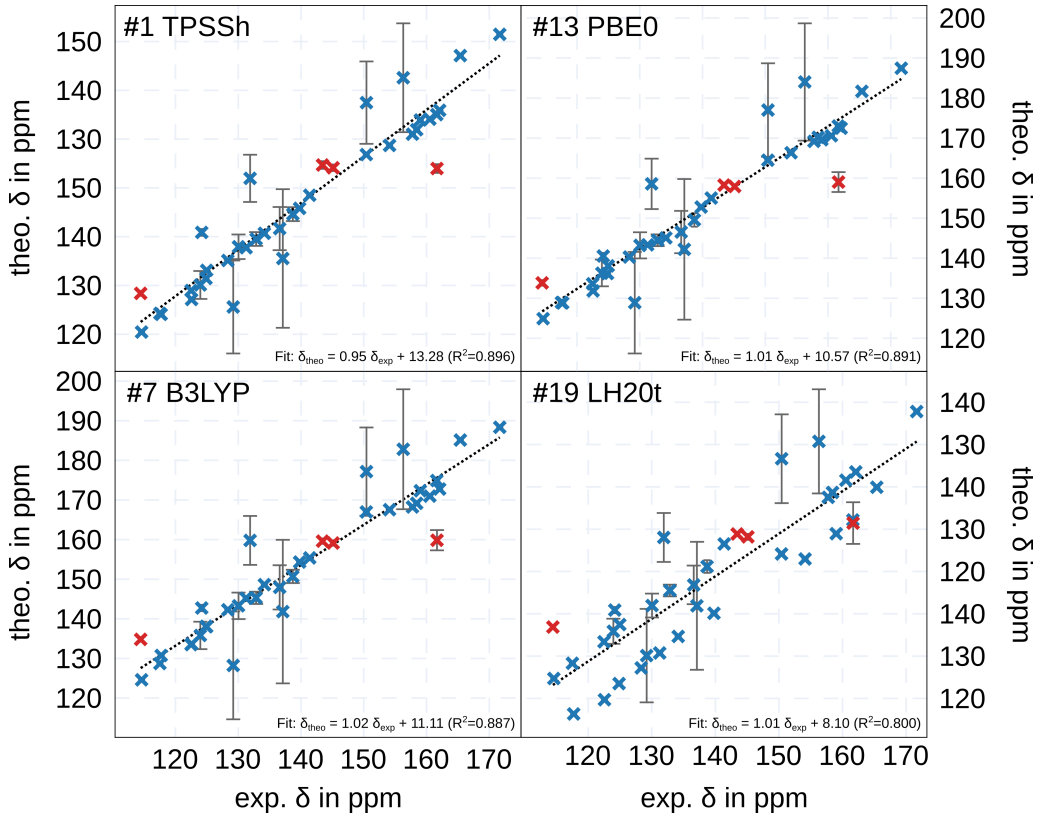

Figure S5: Correlation diagrams comparing calculated and experimentally measured ^{13}C chemical shifts, as summarised in Table S3. Blue crosses denote complexes with a singlet ground state (complexes **1**–**6** and **10**), while red crosses represent complexes with a triplet ground state (complexes **7**–**9**). Error bars indicate the standard deviation of the calculated shifts. The dashed line corresponds to the linear fitted theory–experiment correlation.

This trend confirms previous results [7] (difficulties in predicting) that paramagnetic effects on chemical shifts scale strongly with the proximity to regions of unpaired electron density. In addition, LH20t fails to maintain consistent accuracy across all complexes: in addition to the two challenging cases described above, all five complexes contain carbon positions for which LH20t described poorly. The full set of ^{13}C shifts is provided in Table S4.

Table S3: Summary of all 17 unique experimentally measured and theoretically calculated ^{13}C chemical shifts in the benchmarking set, obtained without relativistic corrections and using the pcSseg-2 basis set. Results correspond to computational protocols #1, #7, #13, and #19 as defined in Table 1 of the main text.

Nr.	Complex	Carbon	Exp.	TPSSh	B3LYP	PBE0	LH20t
2	$[Fe(bpy-4,4'-F)_3]^{2+}$	C_2	162.2[a]	165.9	172.8	172.5	173.5
		C_3	114.6[a]	120.4	124.6	124.9	124.7
		C_4	171.7[a]	181.5	188.3	187.5	187.8
		C_5	117.6[a]	124.3	128.7	128.9	128.3
		C_6	158.5[a]	161.9	169.2	170.2	168.7
3	$[Fe(bpy-4,4'-CF_3)_3]^{2+}$	C_2	160.5[a]	164.1	170.9	170.6	171.6
		C_3	122.5[a]	129.0	133.5	133.6	133.4
		C_4	141.4[a]	148.5	155.4	155.0	156.5
		C_5	125.0[a]	133.1	138.0	138.1	137.5
		C_6	157.8[a]	161.0	168.2	169.2	167.5
5	$[Fe(tpy-ph-4\text{-}F)_2]^{2+}$	C_2	159.0[a]	163.4	172.3	169.6	158.9
		C_3	124.9[a]	131.4	138.1	136.2	123.5
		C_4	139.8[a]	145.8	154.3	152.8	140.1
		C_5	128.3[a]	135.1	142.3	140.3	127.2
		C_6	154.1[a]	158.7	167.5	166.3	153.0
		C_7	160.1[a]	165.0	174.9	173.0	162.2
		C_8	122.6[a]	127.1	133.7	131.8	119.7
		C_9	150.4[a]	156.8	167.0	164.5	154.1
		C_{10}	134.2[a]	140.7	148.6	145.1	134.6
		C_{11}	131.3[a]	137.7	145.2	143.3	130.7
		C_{12}	117.7[a]	124.1	130.7	128.8	116.3
		C_{13}	165.4[a]	177.1	185.1	181.7	169.9
9	$[Fe(pc-F_{16})]$	C_α	161.9[b]	154.0	159.8	159.0	161.4
		C_β	114.9[b]	128.4	134.8	133.8	136.9
		C_γ	143.9[b]	154.7	159.6	158.3	158.9
		C_δ	145.6[b]	154.1	159.1	158.0	158.2
10	$[Fe(phen-(ph-3,5-(CF_3))_2)_3]^{2+}$	C_2	150.4[a]	167.5	177.2	177.0	176.6
		C_3	131.9[a]	152.0	159.8	158.6	158.0
		C_4	137.1[a]	135.5	141.8	142.2	141.9
		C_5	136.6[a]	141.7	147.9	146.5	146.8
		C_6	156.3[a]	172.6	182.8	184.0	180.8
		C_7	130.0[a]	137.9	143.3	143.2	142.0
		C_8	138.7[a]	144.6	150.7	149.6	151.2
		C_9	129.2[a]	125.6	128.2	128.9	130.1
		C_{10}	133.0[a]	139.5	145.3	144.5	145.5
		C_{11}	124.0[a]	130.1	135.8	136.2	135.9
		C_{12}	124.2[a]	140.9	142.7	140.5	140.9

[a] internal Ref., solvent: CD_3CN, this work; [b] internal Ref., solvent: CD_2Cl_2, this work

4 Solvent Dependence of Reference Chemical Shifts

Table S4: Comparison of calculated absolute ^{1}H, ^{13}C, and ^{19}F chemical shifts in ppm of the reference compounds employed in this study. All values were obtained using implicit solvation, the pcSseg-2 basis set, and the LH20t functional according to protocol #19.

Reference	Nucleus	Acetone–d_6	CD_3CN	D_2O	$CDCl_3$
C_6F_6	C	37.75 (8)	37.76 (1)	37.83 (8)	37.7 (31)
	F	355.89 (2)	355.88 (5)	356.00 (8)	355.97 (8)
$CFCl_3$	C	37.529	37.544	37.775	37.513
	F	192.405	192.427	192.707	192.394
$CHCl_3$	C	83.081	83.067	83.309	83.303
	H	23.651	23.652	23.664	23.658
ortho	F'	315.3 (62)	315.3 (62)	315.45 (4)	315.35 (5)
$C_8F_4N_2$	F"	333.18 (6)	333.20 (3)	333.27 (7)	333.07 (6)
TMS	C	191.128	191.128	191.206	191.146)
	H	31.09 (0)	31.09 (1)	31.10 (4)	31.09 (2)

To assess the uncertainty introduced by employing implicit solvation models (COSMO/CPCM) instead of explicit solvation approaches, we analysed the solvent dependence of absolute NMR chemical shifts for the reference compounds analysed in this study. Specifically, we considered ^{1}H shifts of $CHCl_3$ and TMS, ^{13}C shifts of C_6F_6, $CFCl_3$, $CHCl_3$, and TMS, as well as ^{19}F shifts of $CFCl_3$ and ortho-$C_8F_4N_2$.

As summarized in Table S4, the variations induced by different implicit solvents are very small. For ^{1}H shifts, the maximum deviation is below 0.01 ppm. For ^{13}C shifts, the observed solvent dependence ranges from 0.13 ppm for C_6F_6 up to 0.22 ppm for $CHCl_3$. Similarly, the ^{19}F shifts vary between 0.12 ppm for C_6F_6 and 0.31 ppm for $CFCl_3$.

For comparison, experimentally observed solvent effects are substantially larger. Reported literature values for $CHCl_3$ show ^{1}H chemical shifts ranging from 6.15 ppm in C_6D_6 to 8.02 ppm in acetone–d_6, while the corresponding ^{13}C shifts span 77.4 ppm in $CDCl_3$ to 79.2 ppm in acetone–d_6.[8] For C_6F_6, literature data[9] report ^{19}F chemical shifts between -165.37 ppm in CD_3OD and -161.64 ppm in $CDCl_3$.

These experimentally observed variations are approximately one order of magnitude

larger for ^{13}C and ^{19}F, and two orders of magnitude larger for ^{1}H, than the differences obtained using implicit solvation models. The pronounced solvent dependence of ^{1}H and ^{13}C chemical shifts highlights inherent limitations of implicit solvation approaches, which neglect specific solute–solvent interactions such as steric effects and hydrogen bonding. Consequently, explicit solvation models are expected to become essential when addressing subtle spectral features, including small chemical shift differences arising from facial/meridional isomerism, and should be explored in future work.

5 Experimental NMR, IR & UV/Vis-Spectra

5.1 NMR sample preparation

For NMR spectroscopy, all complexes were dissolved in 0.5 mL deuterated solvent with concentrations given in table S5 below. To the solvents 3 mg to 9 mg hexafluorobenzene as an internal chemical shift reference were added, resulting in concentrations below 0.1 M, as recommended by Rosenau *et al.*.[9] Referencing was done by setting the residual solvent signal (^{1}H, ^{13}C) or C_6F_6 signal (for ^{19}F) to the values listed in table S5. The influence of the aromatic additive on the chemical shift of the analytes is minimal, as shown by the direct comparison of solutions of complex **3** with internal (added to the solution) and external C_6F_6 (added as solution in a coaxial insert) in figure S6.

Table S5: Details about sample composition and the signals used for referencing.

Nr.	Complex	Concentration	Solvent	Reference signal	δ (ppm)
2	$[Fe(bpy-4,4'-F)_3]^{2+}$	12 mM	CD_3CN	$CH\mathbf{H}D_2CN$	1.94[a]
				$\mathbf{C}D_3CN$	1.32[a,b]
				$C_6\mathbf{F}_6$	-164.38[c]
3	$[Fe(bpy-4,4'-CF_3)_3]^{2+}$	16 mM	CD_3CN	$CH\mathbf{H}D_2CN$	1.94[a]
				$\mathbf{C}D_3CN$	1.32[a,b]
				$C_6\mathbf{F}_6$	-164.38[c]
5	$[Fe(tpy-ph-4\text{-}F)_2]^{2+}$	13 mM	CD_3CN	$CH\mathbf{H}D_2CN$	1.94[a]
				$\mathbf{C}D_3CN$	1.32[a,b]
				$C_6\mathbf{F}_6$	-164.38[c]
8	$[Fe(tpp-F_{20})]$	1.5 mM	toluene-d_8	$C_6\mathbf{F}_6$	-163.33[c]
9	$[Fe(pc-F_{16})]$	3 mM	CD_2Cl_2	$\mathbf{C}D_2Cl_2$	53.84[d]
				$C_6\mathbf{F}_6$	-162.61[c]
10	$[Fe(phen-(ph-3,5-(CF_3))_2)_3]^{2+}$	1.5 mM	CD_3CN	$CH\mathbf{H}D_2CN$	1.94[a]
				$\mathbf{C}D_3CN$	1.32[a,b]
				$C_6\mathbf{F}_6$	-164.38[c]

[a] Values taken from Ref.[10] ; [b] Methyl carbon is used as reference.; [c] Values taken from Ref.[9] ; [d] Values taken from Ref.[8]

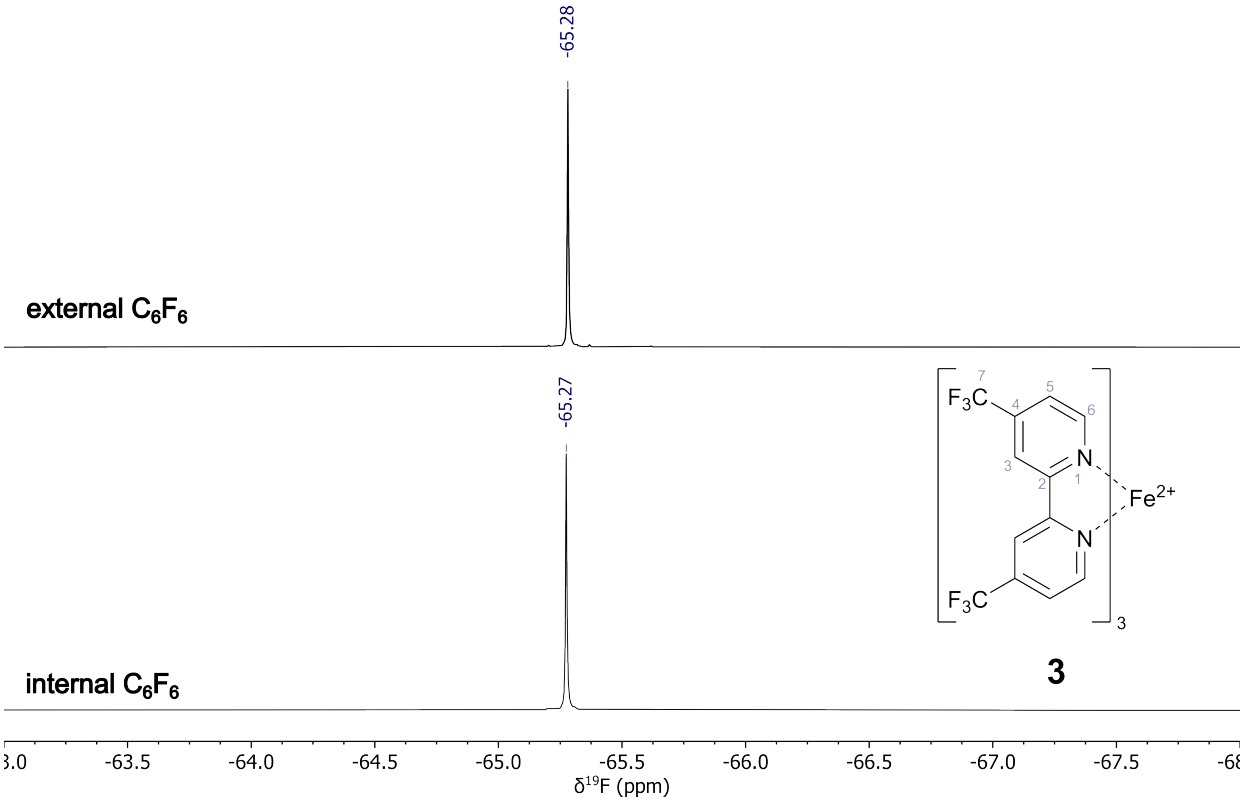

Figure S6: ^{19}F spectra and chemical shift values of complex **3**, using externally (as solution in coaxial insert; top) and internally applied C_6F_6 as reference (added to the solution; bottom). The selected region shows the signal of fluorine atoms F7 in complex **3**.

5.2 Complex 2 - $[Fe(bpy-4,4'-F)_3]^{2+}$

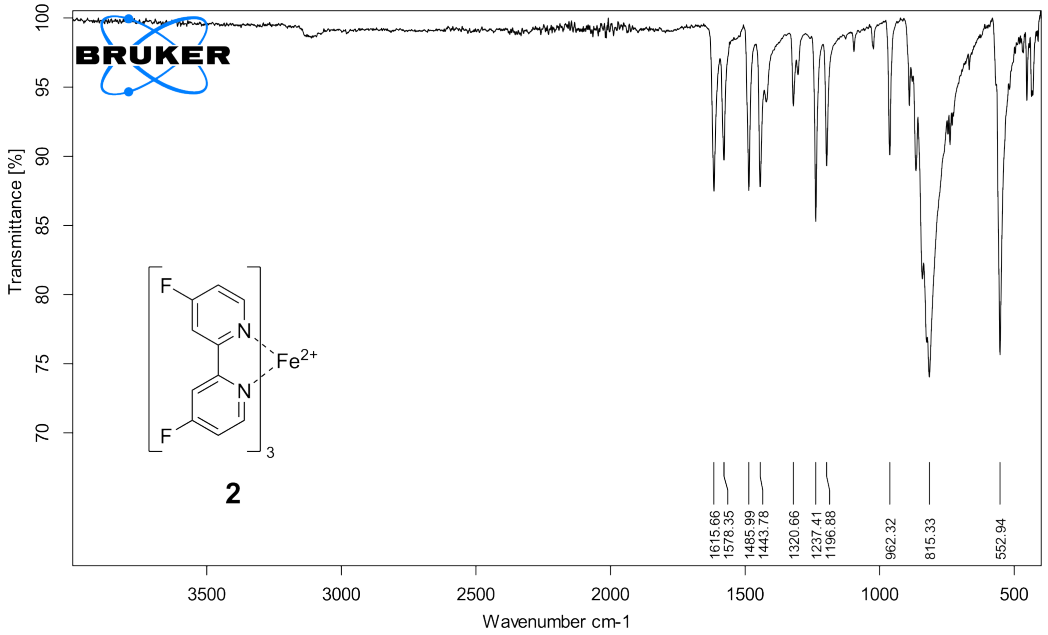

Figure S7: IR spectrum of complex **2**.

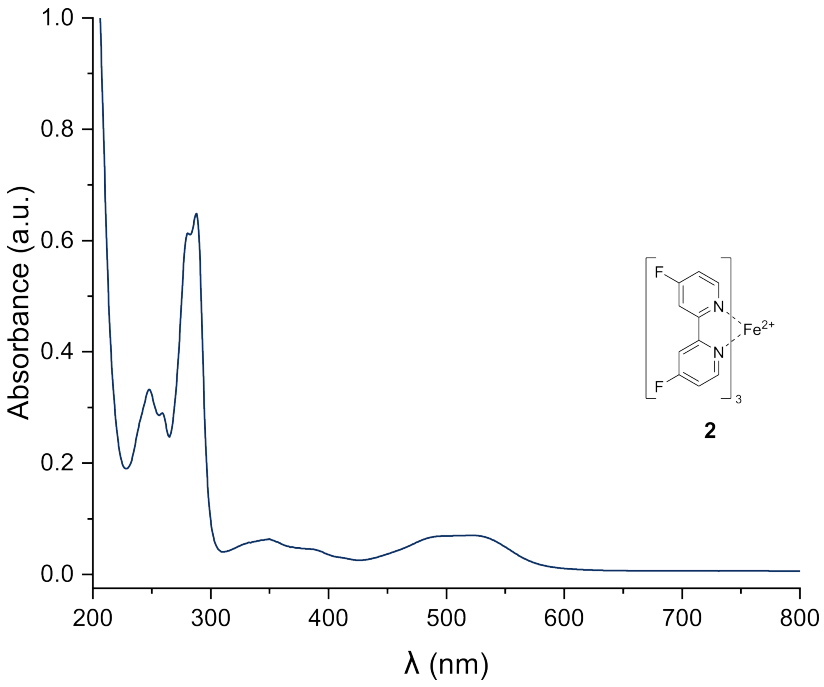

Figure S8: UV/vis spectrum of complex **2** in CH_3CN (0.09 mM).

^{1}H NMR (700 MHz, CD_3CN): δ = 8.37 (dd, J = 8.7, 2.7 Hz, $6H_3$), 7.46 (pseudo-t, J = 6.5 Hz, $6H_6$), 7.32 (pseudo-td, J = 6.8, 2.7 Hz, $6H_5$) ppm.

^{13}C NMR (176 MHz, CD_3CN): δ = 171.68 (d, J = 267 Hz, C_4), 162.20 (dd, J = 9.3, 3.3 Hz, C_2), 158.52 (d, J = 9.7 Hz, C_6), 117.60 (d, J = 20 Hz, C_5), 114.68 (d, J = 23 Hz, C_3) ppm.

^{19}F NMR (659 MHz, CD_3CN): δ = -72.82 (d, J = 707 Hz, $12F_{PF_6^-}$), -98.52 (d-pseudo-t, J = 7.7, 7.4 Hz, $6F_4$) ppm.

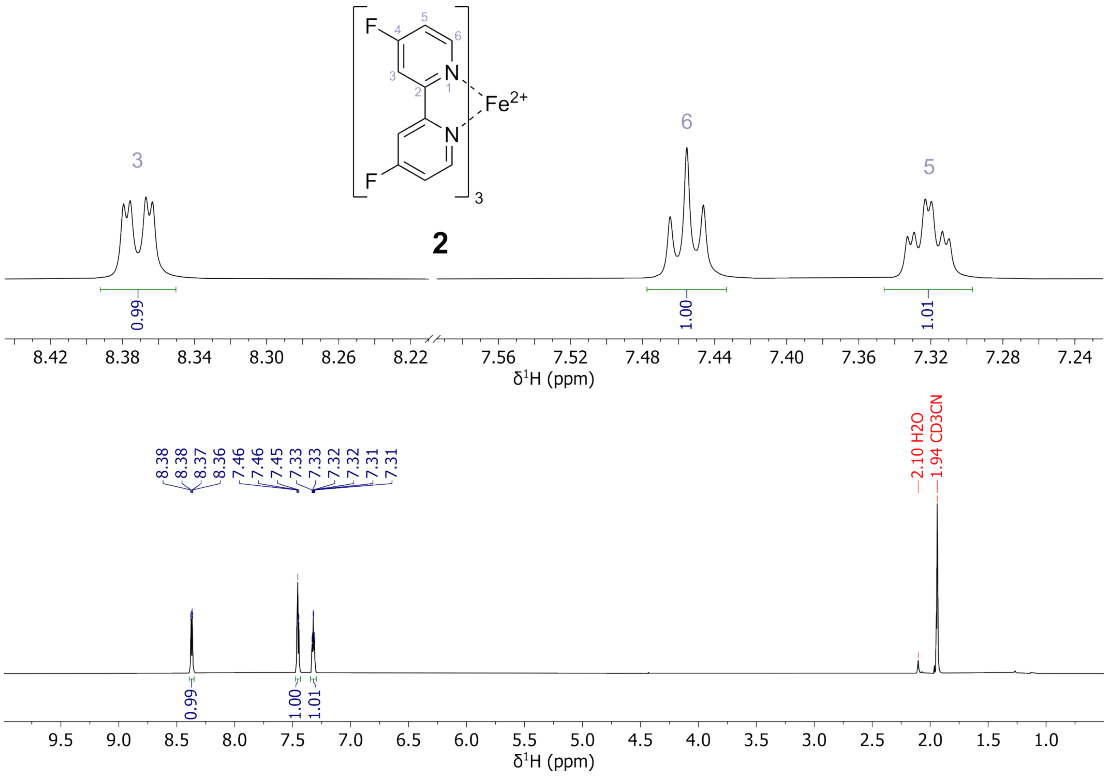

Figure S9: ^{1}H NMR spectrum of complex **2** in CD_3CN at 300 K.

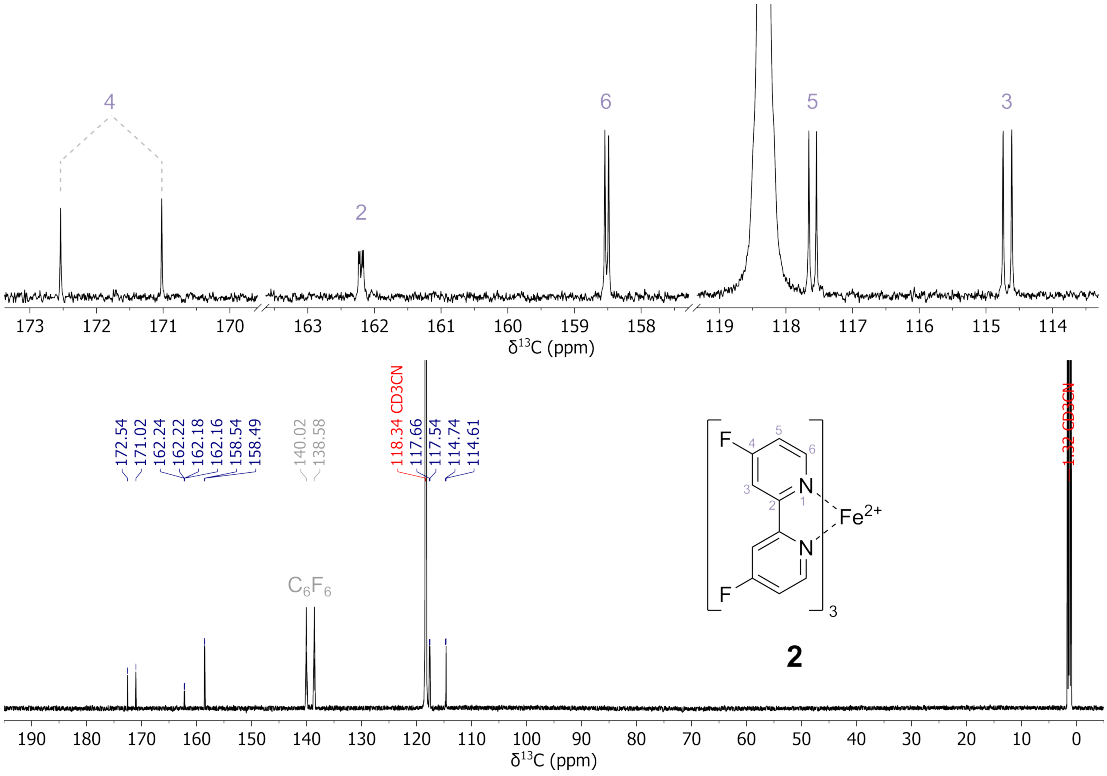

Figure S10: ^{13}C NMR spectrum of complex **2** in CD_3CN at 300 K.

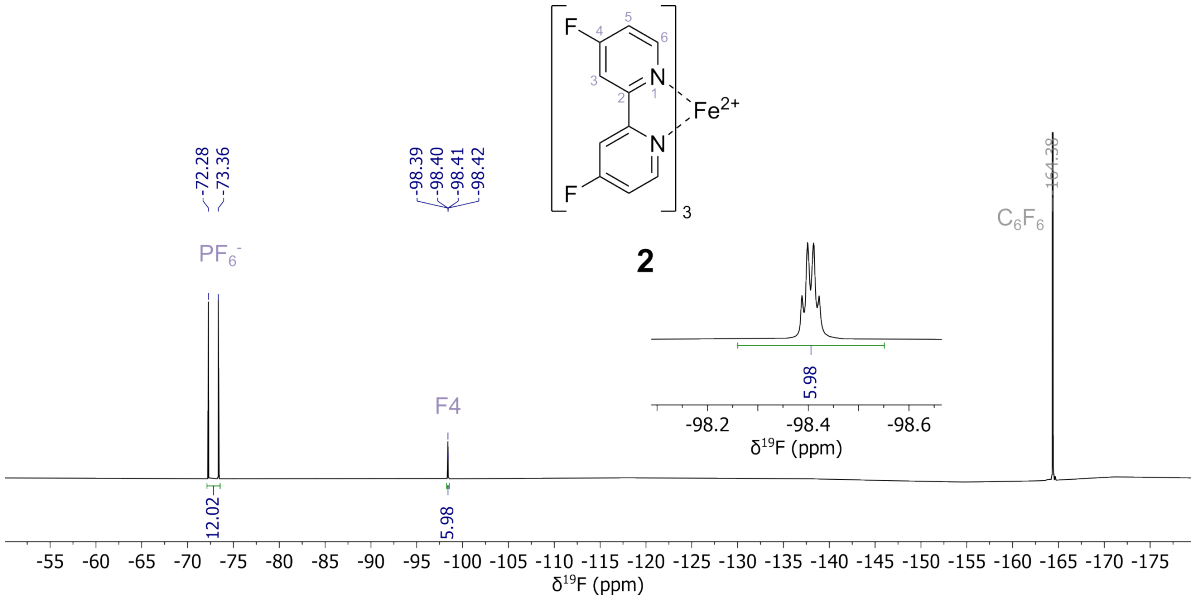

Figure S11: ^{19}F NMR spectrum of complex **2** in CD_3CN at 300 K.

MS (HR-ESI, m/z): $[M]^{2+}$ calculated for $[C_{30}H_{18}F_6FeN_6]$ 316.04180; found 316.04168 (Δ = 0.38 ppm).

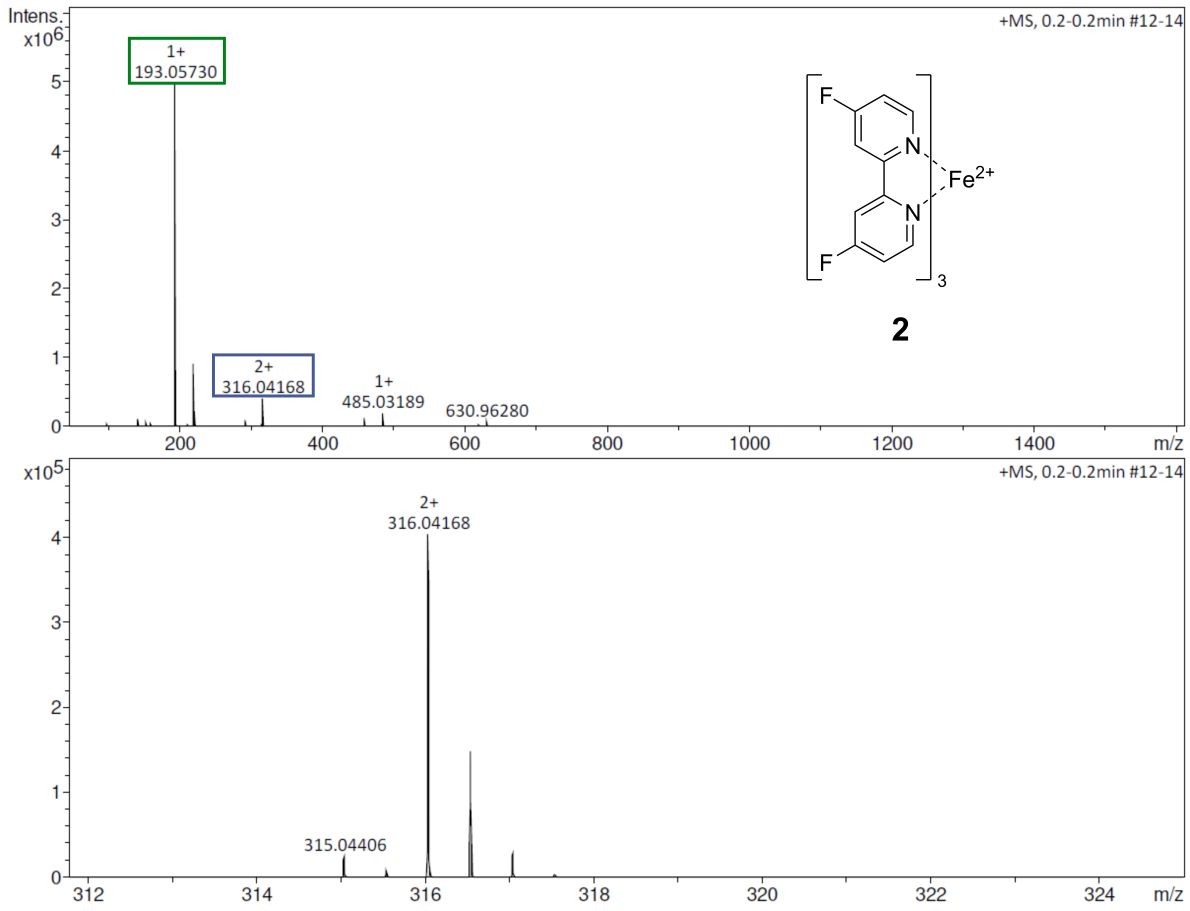

Figure S12: High-resolution mass spectrum of complex **2** acquired as ESI in positive ionisation mode. The double positive charged complex cation is marked in blue, the ligand $[H^+]$ in green.

5.3 Complex 3 - $[Fe(bpy-4,4'-CF_3)_3]^{2+}$

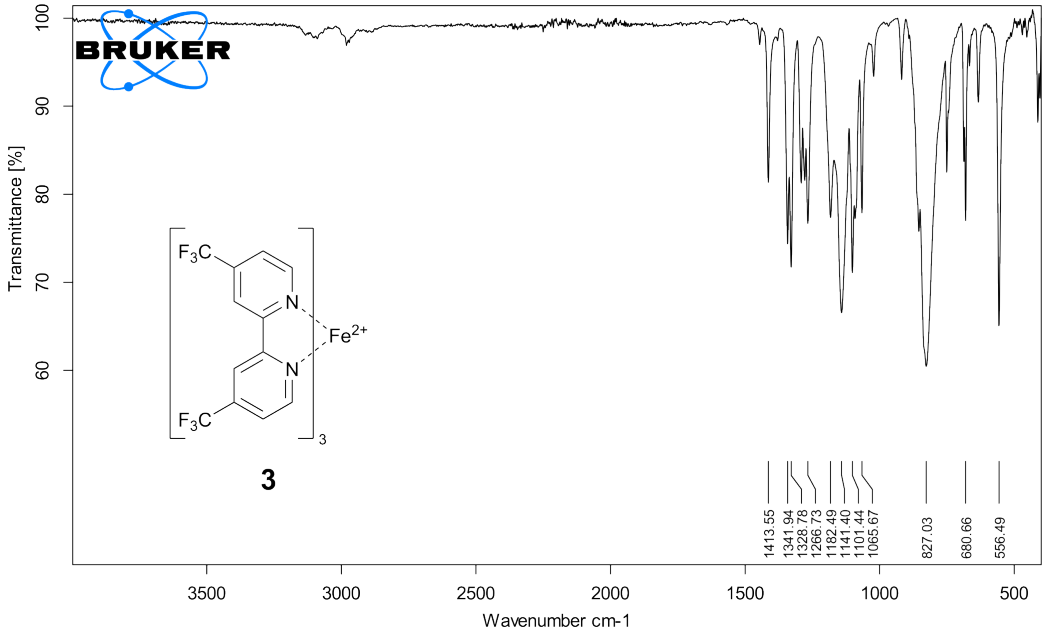

Figure S13: IR spectrum of complex **3**.

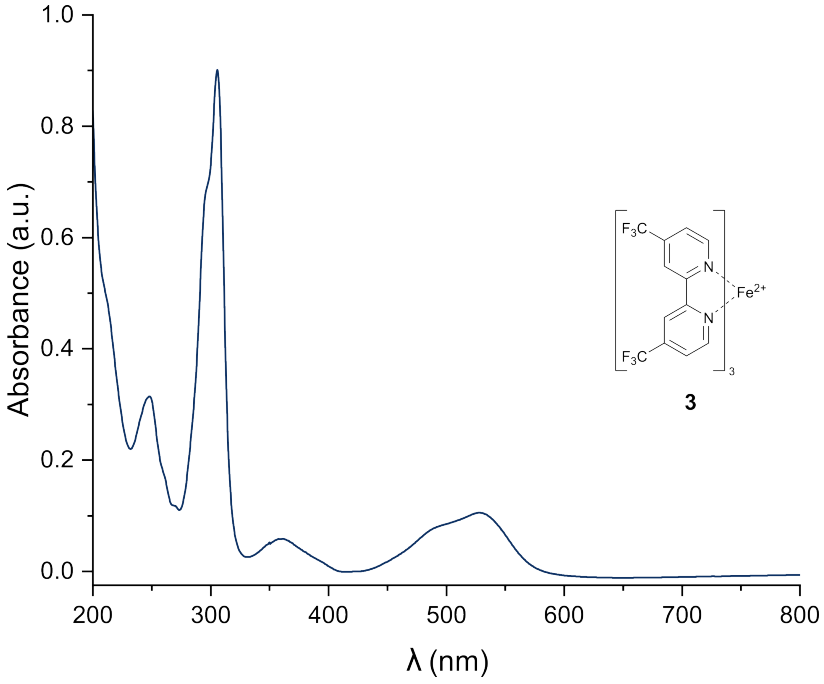

Figure S14: UV/vis spectrum of complex **3** in CH_3CN (0.13 mM).

^{1}H NMR (700 MHz, CD_3CN): δ = 8.98 (s, $6H_3$), 7.71 (d, J = 5.5 Hz, $6H_5$), 7.66 (d, J = 5.5 Hz, $6H_6$) ppm.

^{13}C NMR (176 MHz, CD_3CN): δ = 160.53 (C_2), 157.76 (C_6), 141.39 (q, J = 35.6 Hz, C_4), 124.97 (q, J = 3.3 Hz, C_5), 123.33 (q, J = 273 Hz, C_7), 122.49 (q, J = 3.4 Hz, C_3) ppm.

^{19}F NMR (659 MHz, CD_3CN): δ = -65.27 (s, $18F_7$), -72.84 (d, J = 706 Hz, $12F_{PF_6^-}$) ppm.

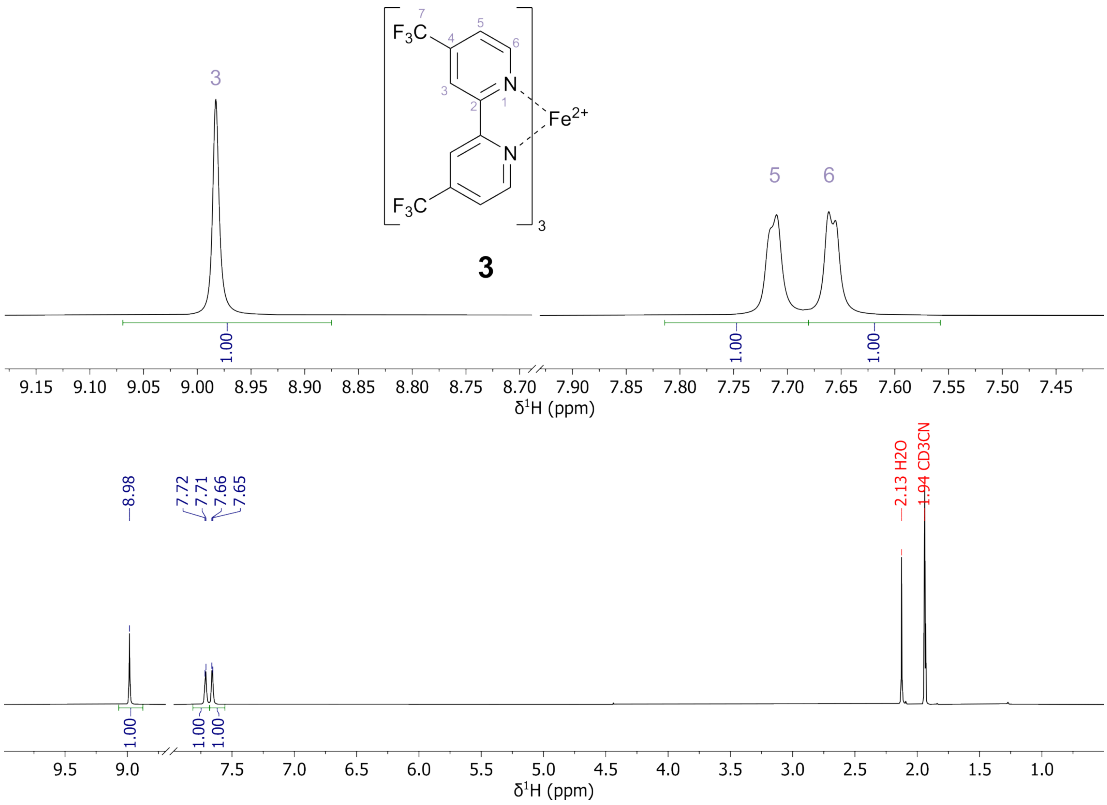

Figure S15: ^{1}H NMR spectrum of complex **3** in CD_3CN at 300 K.

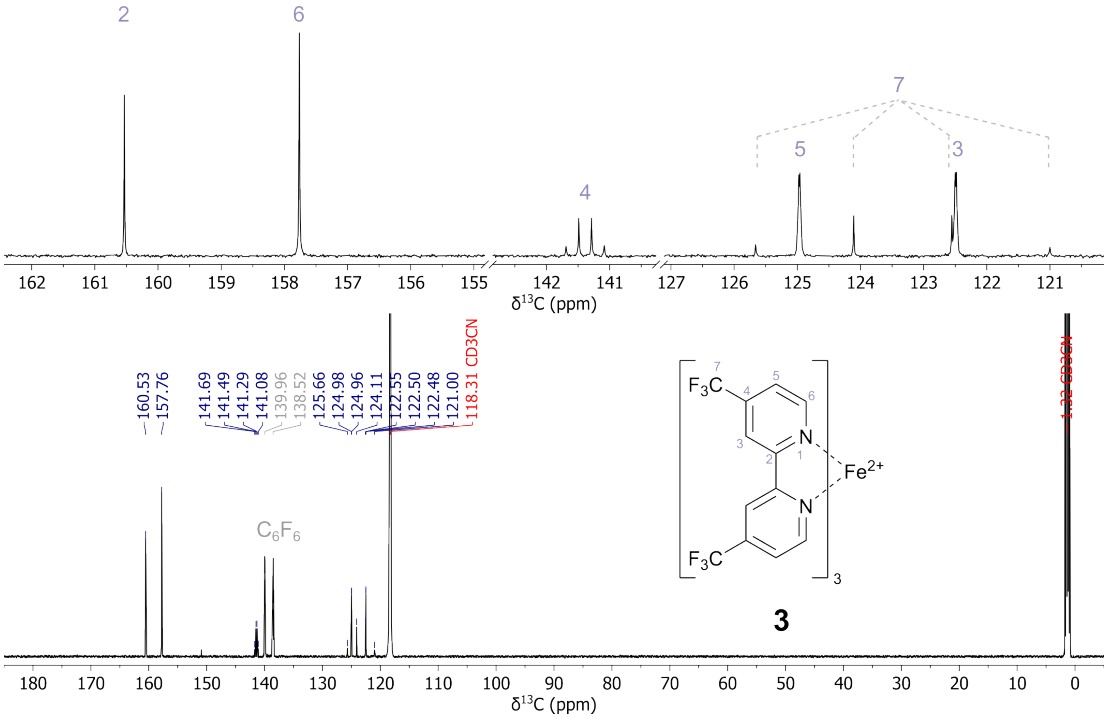

Figure S16: ^{13}C NMR spectrum of complex **3** in CD_3CN at 300 K.

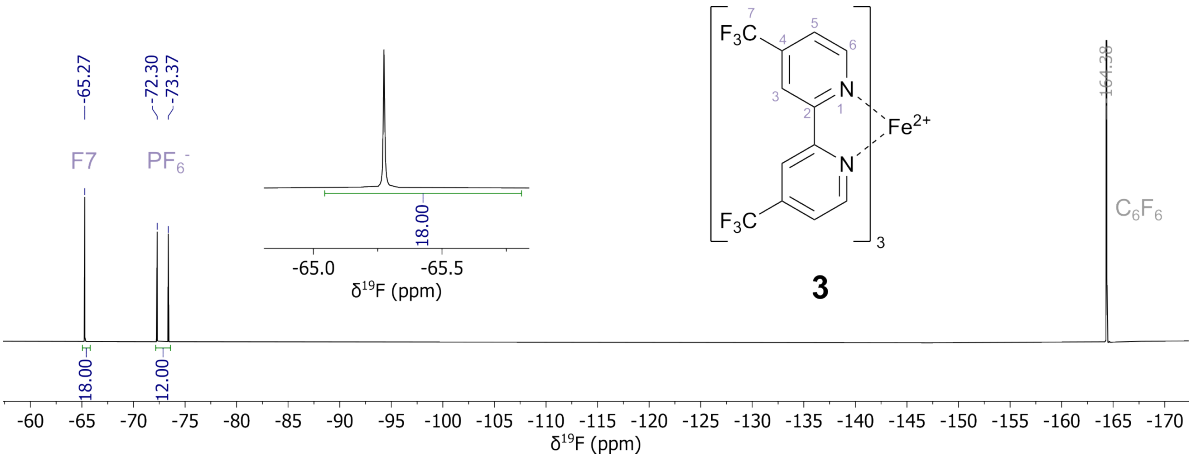

Figure S17: ^{19}F NMR spectrum of complex **3** in CD_3CN at 300 K.

MS (HR-ESI, m/z): $[M]^{2+}$ calculated for $[C_{36}H_{18}F_{18}FeN_6]$ 466.03222; found 466.03246 (Δ = 0.49 ppm).

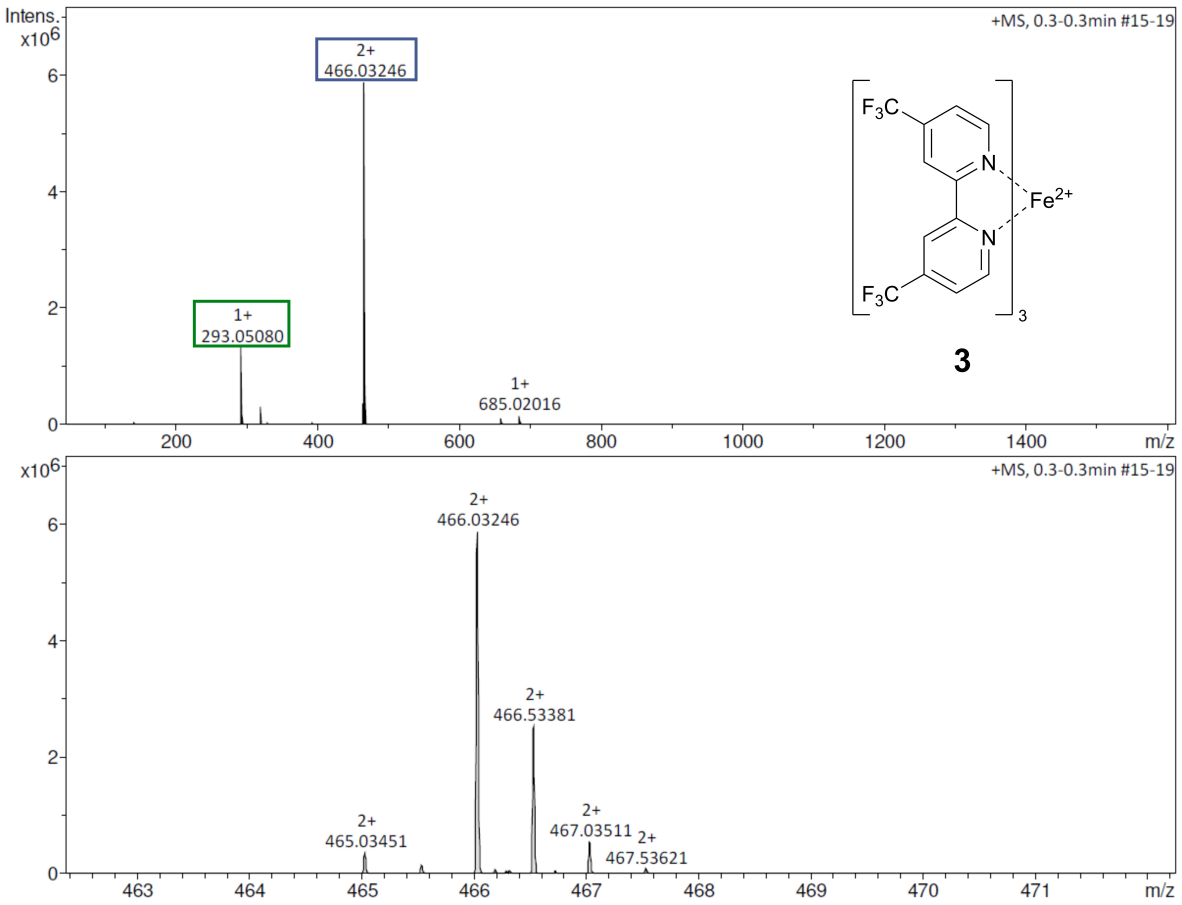

Figure S18: High-resolution mass spectrum of complex **3** acquired as ESI in positive ionisation mode. The double positive charged complex cation is marked in blue, the ligand $[H^+]$ in green.

5.4 Complex 5 - $[Fe(tpy-ph-4\text{-}F)_2]^{2+}$

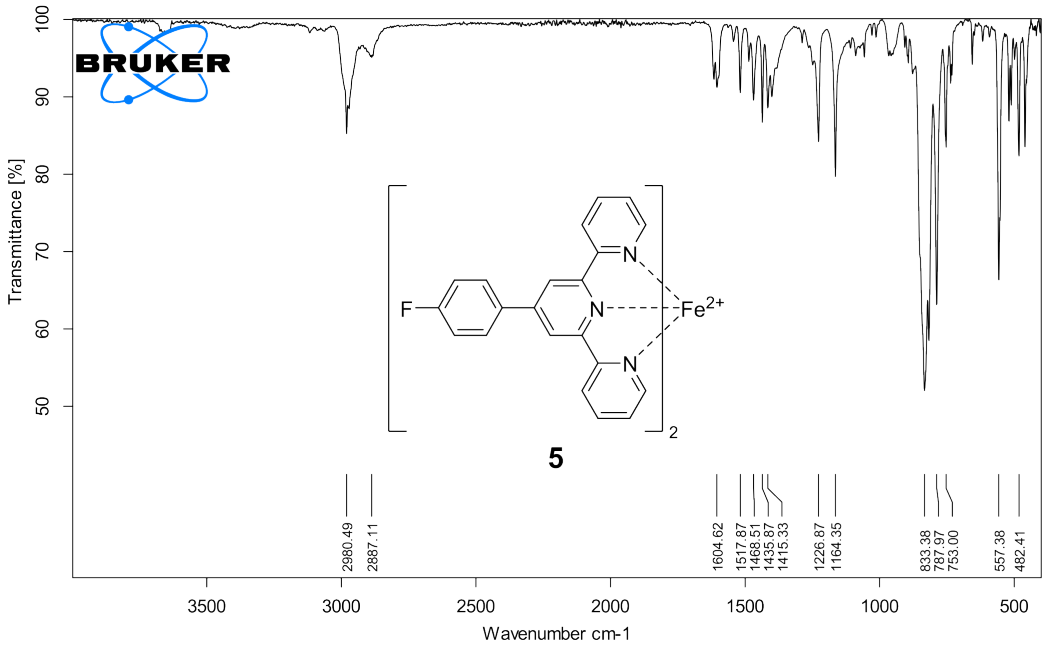

Figure S19: IR spectrum of complex **5**.

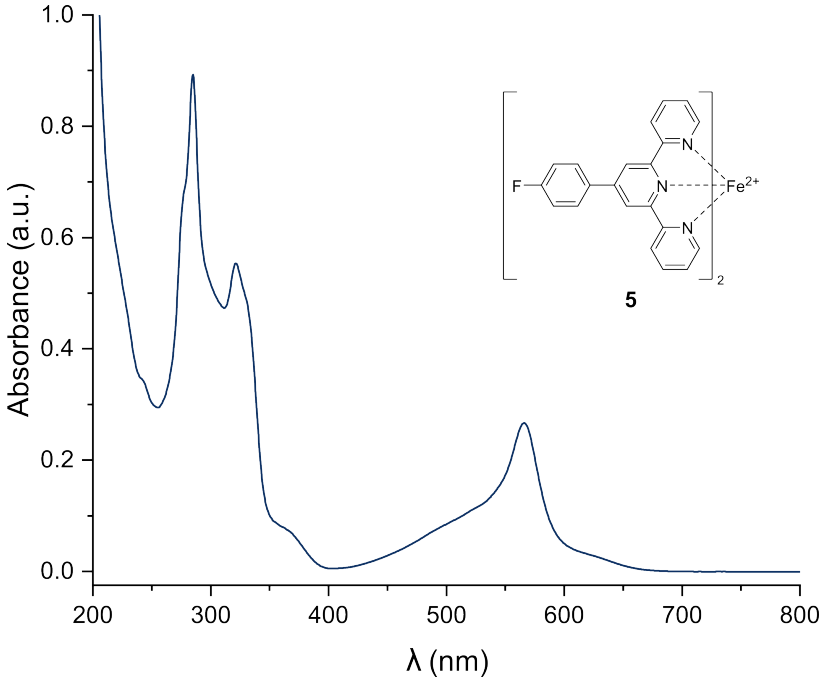

Figure S20: UV/vis spectrum of complex **5** in CH_3CN (0.09 mM).

^{1}H NMR (700 MHz, CD_3CN): δ = 9.15 (s, $4H_9$), 8.60 (d, J = 7.9 Hz, $4H_3$), 8.35 (m, $4H_{12}$), 7.91 (pseudo-td, J = 7.7, 1.4 Hz, $4H_4$), 7.57 (m, $4H_{13}$), 7.19 (d, J = 5.6 Hz, $4H_6$), 7.09 (ddd, J = 7.2, 5.6, 1.4 Hz, $4H_5$) ppm.

^{13}C NMR (176 MHz, CD_3CN): δ = 165.39 (d, J = 250 Hz, C_{14}), 161.36 (C_8), 159.01 (C_2), 154.11 (C_6), 150.41 (C_{10}), 139.78 (C_4), 134.16 (d, J = 3.2 Hz, C_{11}), 131.25 (d, J = 8.8 Hz, C_{12}), 128.34 (C_5), 124.86 (C_3), 122.56 (C_9), 117.72 (d, J = 22 Hz, C_{13}) ppm.

^{19}F NMR (659 MHz, CD_3CN): δ = -72.82 (d, J = 706 Hz, $12F_{PF_6^-}$), -111.79 (tt, J = 8.9, 5.0 Hz, $2F_{14}$) ppm.

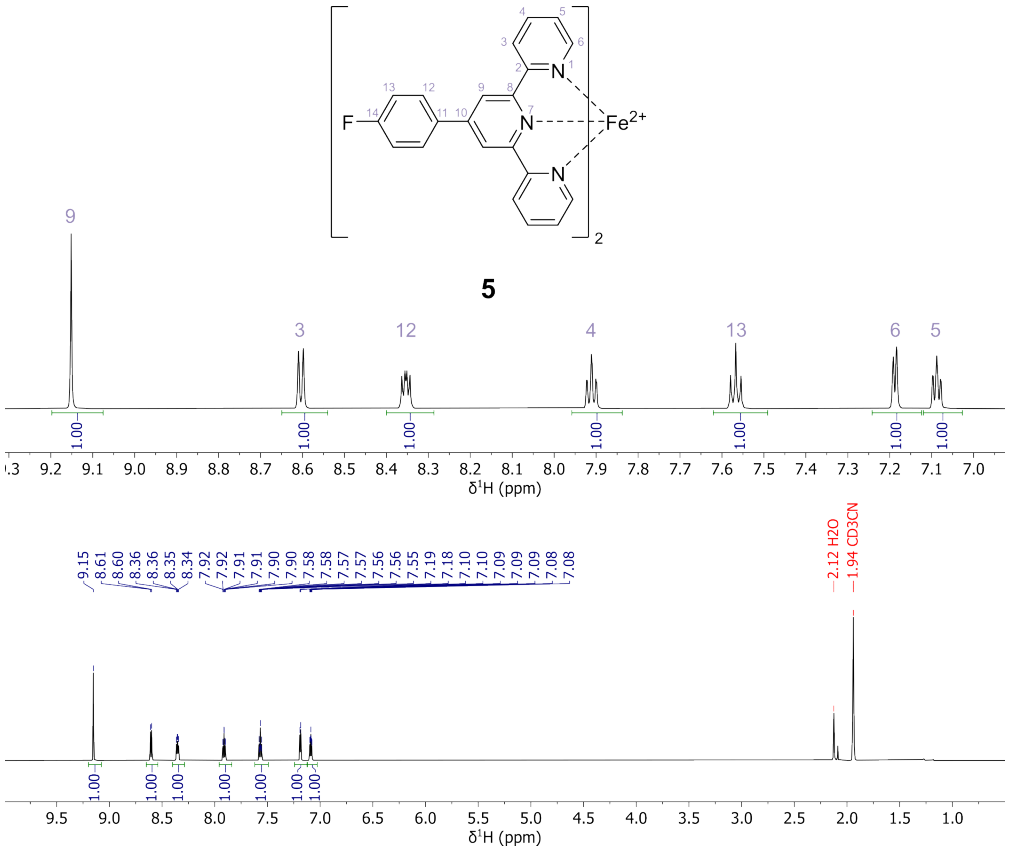

Figure S21: ^{1}H NMR spectrum of complex **5** in CD_3CN at 300 K.

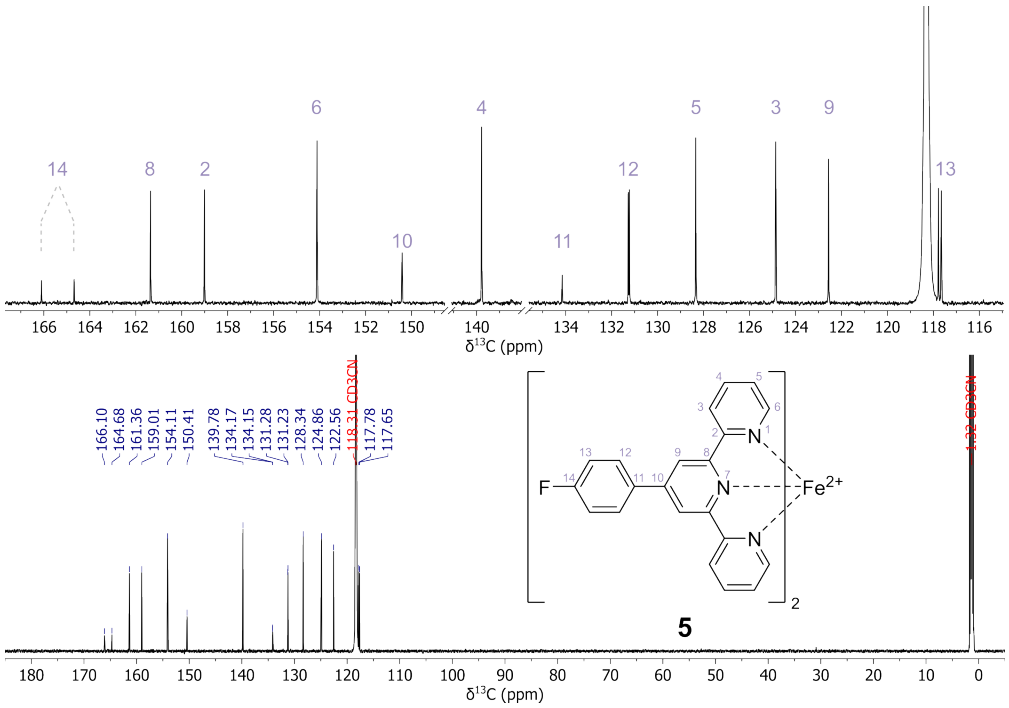

Figure S22: ^{13}C NMR spectrum of complex **5** in CD_3CN at 300 K.

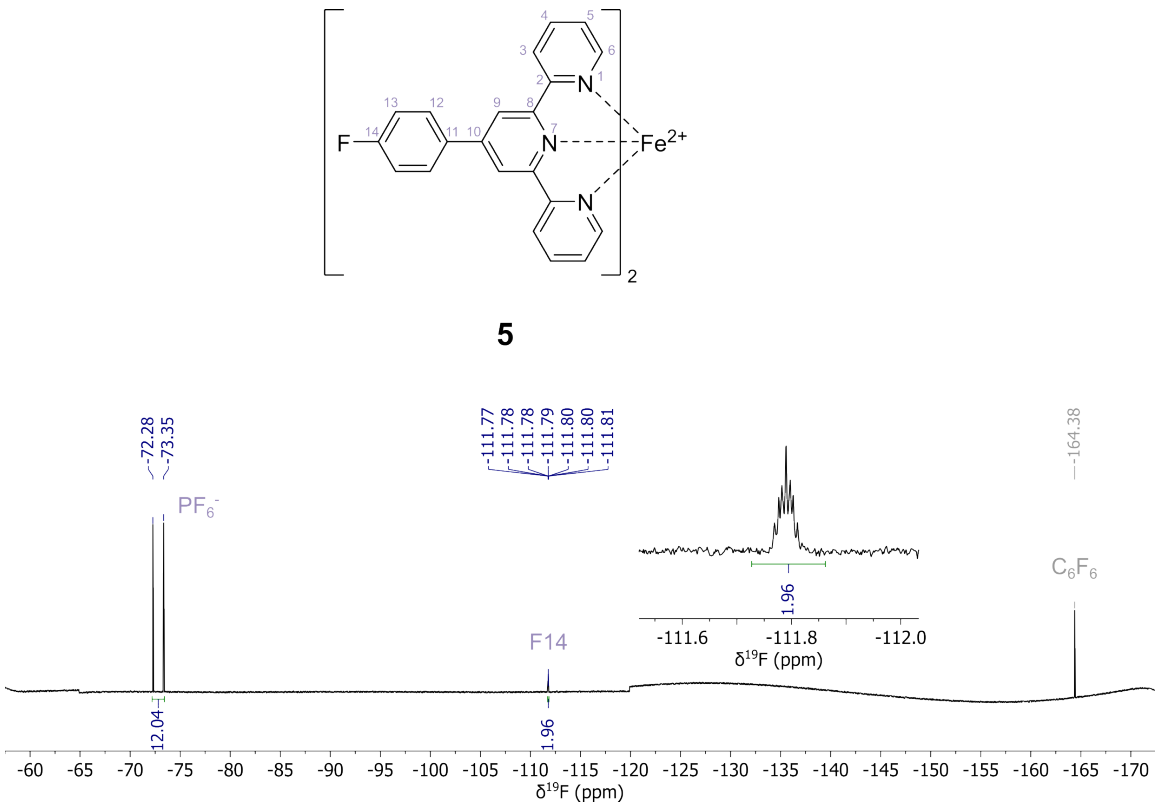

Figure S23: ^{19}F NMR spectrum of complex **5** in CD_3CN at 300 K. Baseline correction was only applied to the range from -65 ppm to -120 ppm.

MS (HR-ESI, m/z): $[M]^{2+}$ calculated for $C_{42}H_{28}F_2FeN_6$ 355.08413; found 355.08378 (Δ = 0.99 ppm).

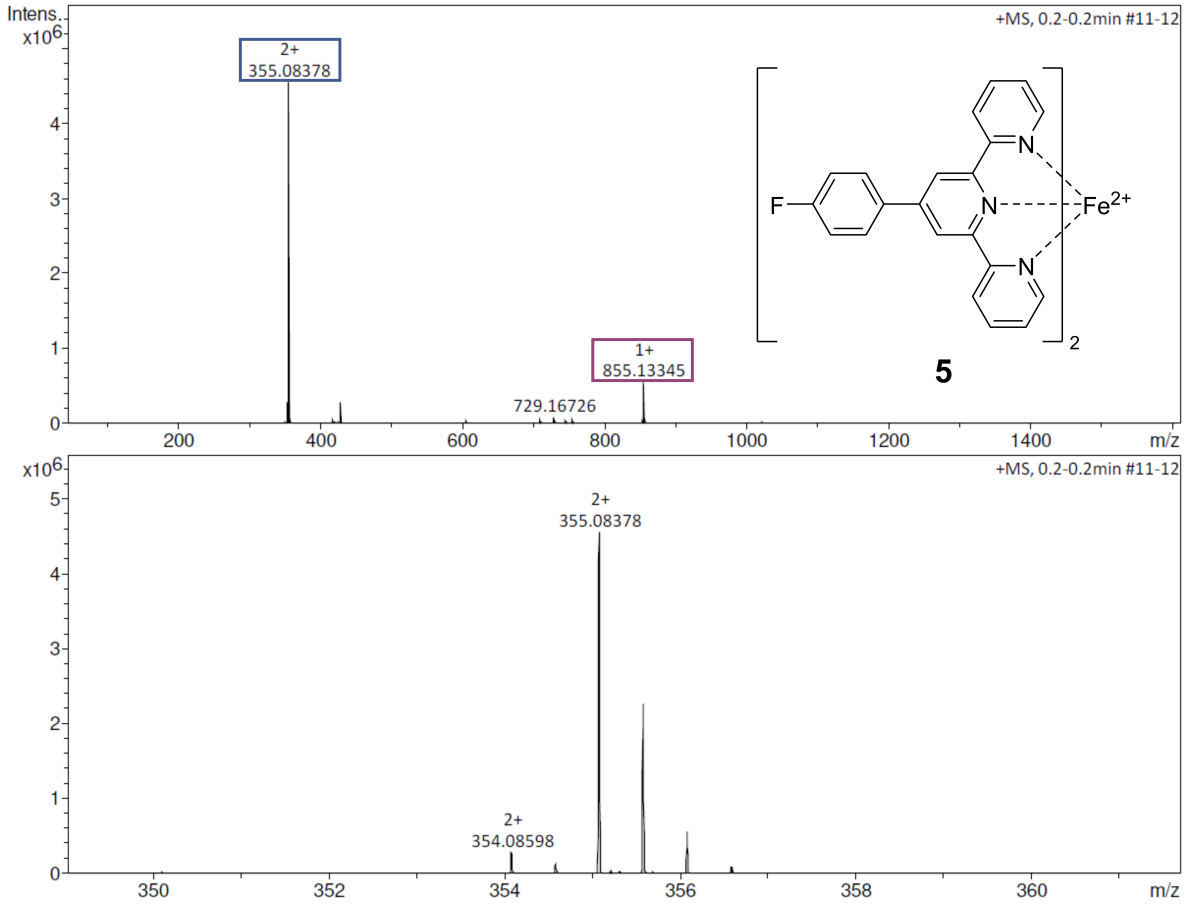

Figure S24: High-resolution mass spectrum of complex **5** acquired as ESI in positive ionisation mode. The double positive charged complex cation is marked in blue, the complex cation with one PF_6^- anion in magenta.

5.5 Complex 8 - [Fe(tpp−F_{20})]

^{19}F NMR (659 MHz, toluene-d_8): δ = -136.97 (br, 8F_o), -152.06 (br, 4F_p), -161.46 (br, 8F_m) ppm.

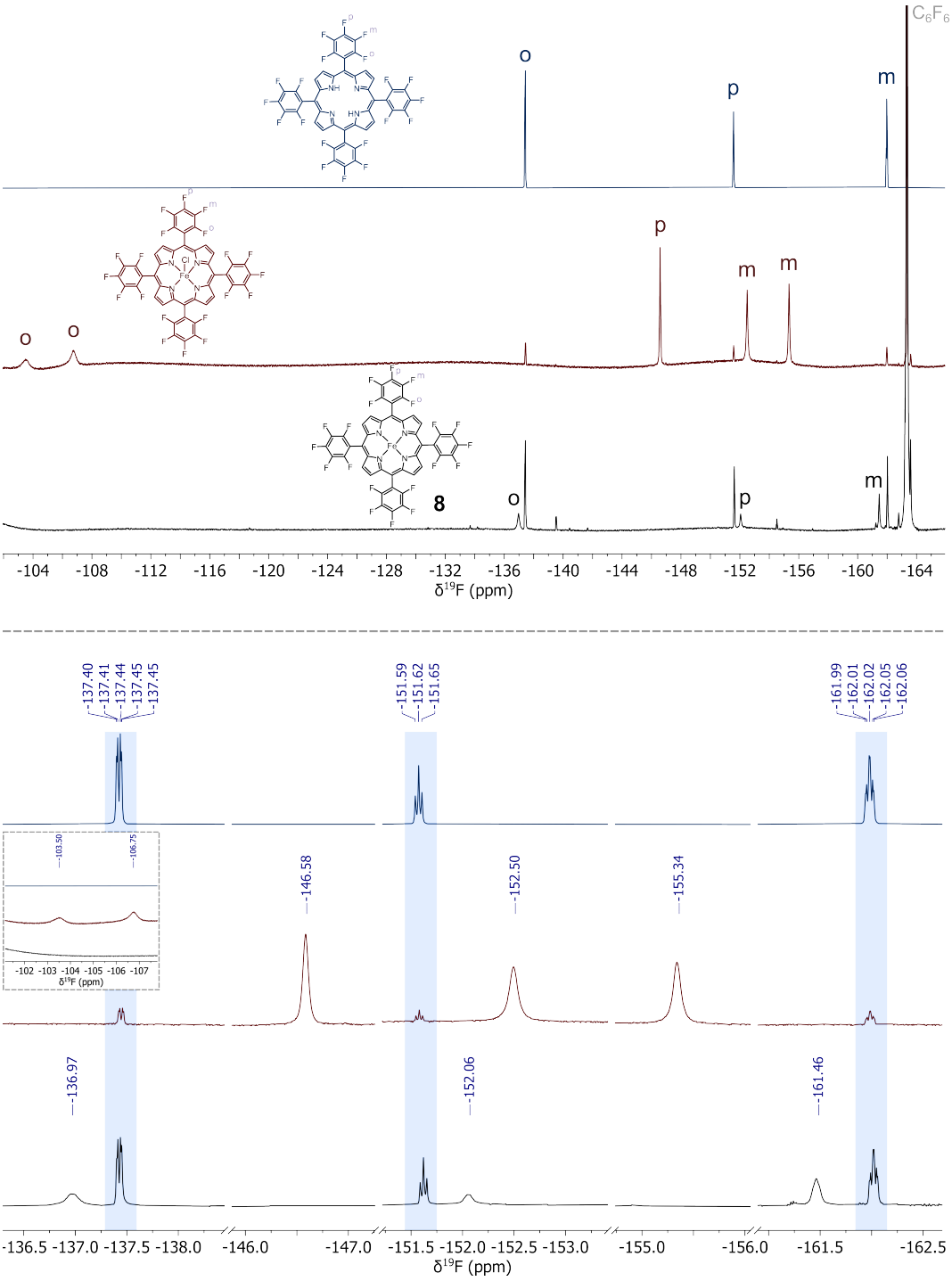

Figure S25: ^{19}F NMR spectrum of complex **8** (black) in toluene-d8 at 300 K, along with the free ligand (blue) and the chlorinated iron complex (red). **8** was generated *in situ* from the chloroiron compound in the NMR tube. Some free ligand remained in the sample and is indicated by coloured boxes. The chemical shifts of all species match those reported in literature, with the iron complexes signals being slightly broadened due to their (paramagnetic) spin state.[6]

5.6 Complex 9 - [Fe(pc−F_{16})]

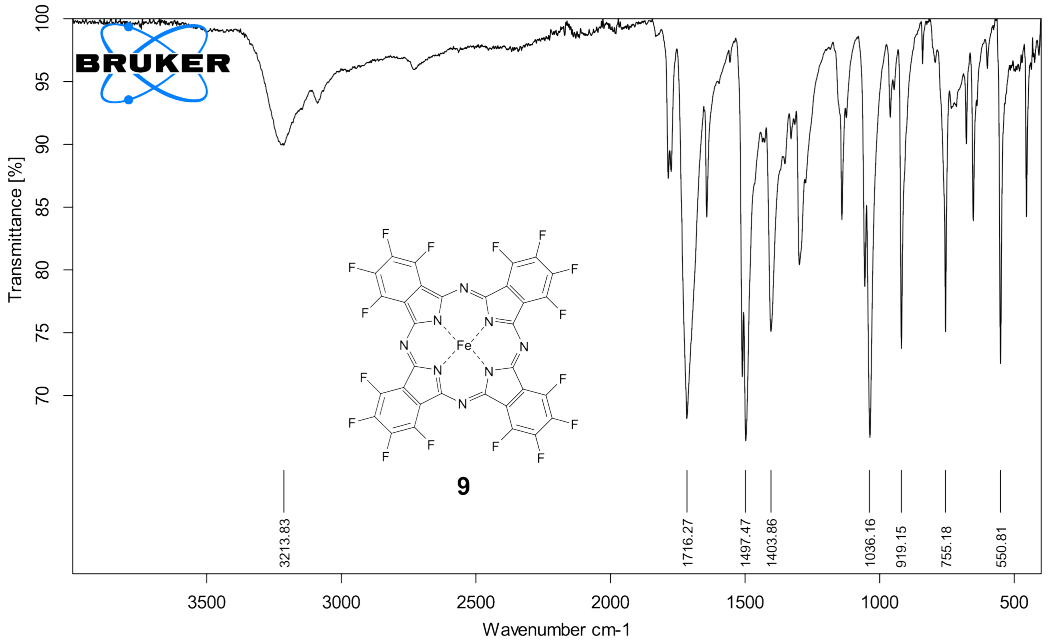

Figure S26: IR spectrum of complex **9**.

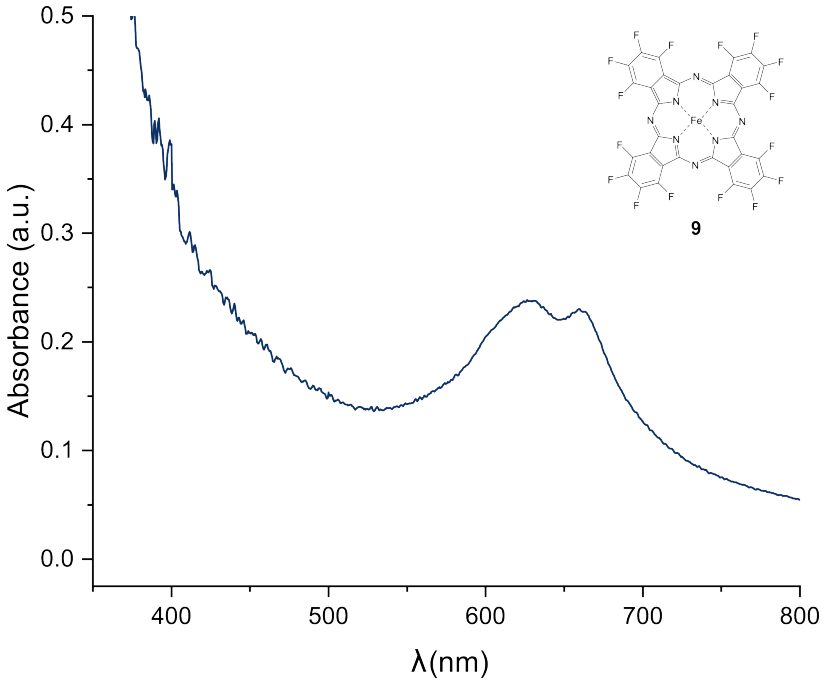

Figure S27: UV/vis spectrum of complex **9** in acetone (saturated solution $<$ 1 mM).

{^{19}F}^{13}C NMR (176 MHz, CD_2Cl_2): δ = 161.94 (C_4), 145.57 (C_1), 143.88 (C_2), 114.89 (C_3) ppm.

^{19}F NMR (659 MHz, CD_2Cl_2): δ = -136.34 (m, $8F_2$), -142.71 (m, $8F_1$) ppm.

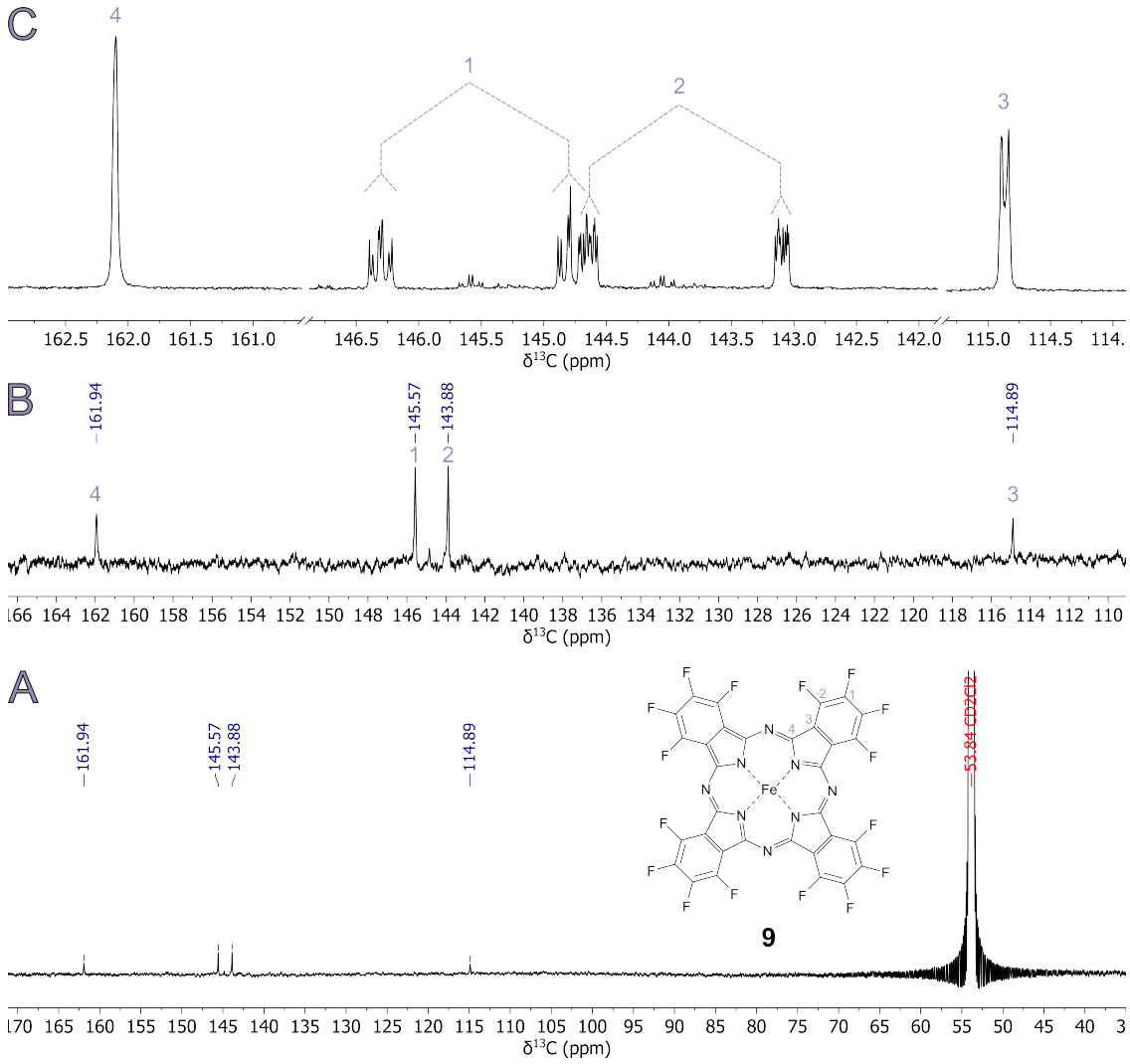

Figure S28: ^{19}F-decoupled {^{19}F}^{13}C NMR spectrum of complex **9** in CD_2Cl_2 at 300 K (**A** and **B**). Proton-decoupled {^{1}H}^{13}C spectrum of a different sample (**C**). Here, the ^{13}C-^{19}F coupling pattern allows for signal assignment.

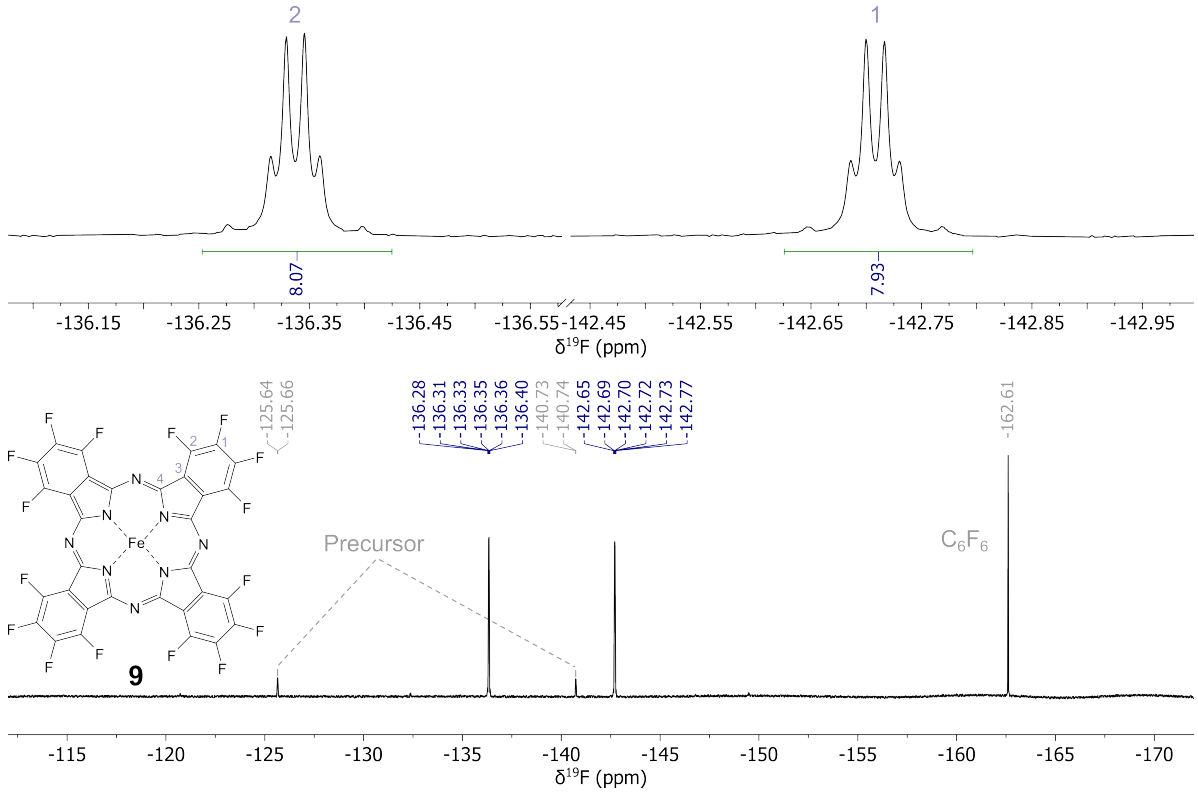

Figure S29: ^{19}F NMR spectrum of complex **9** in CD_2Cl_2 at 300 K. Some remaining tetrafluorophthalodinitrile precursor can be seen.

MS (HR-APCI, *m/z*): [M+H] calculated for 856.94130; found 856.93925 (Δ = -2.34 ppm).

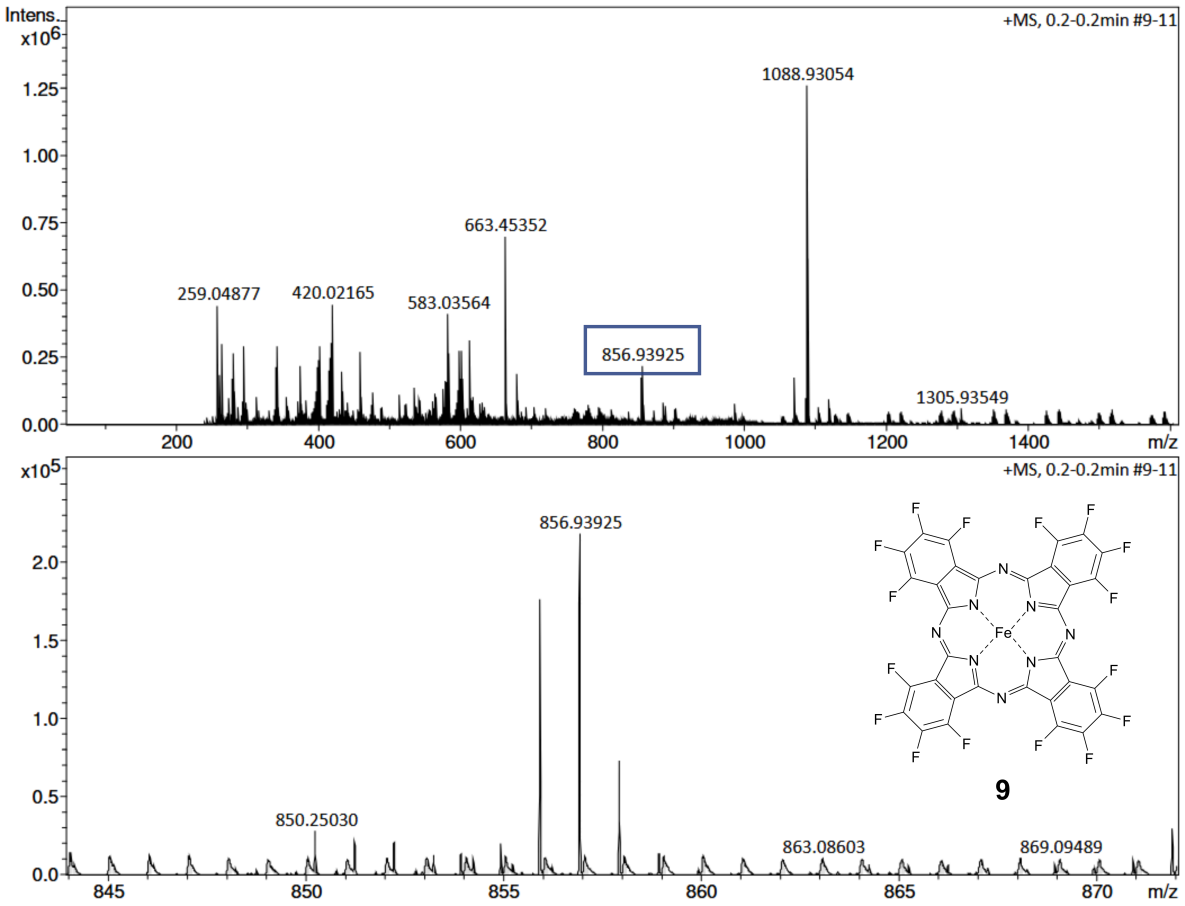

Figure S30: High-resolution mass spectrum of complex **9** acquired as APCI in positive ionisation mode. The complex cation of **9** is marked in blue.

5.7 Complex 10 - $[Fe(phen-(ph-3,5-(CF_3)))_3]^{2+}$

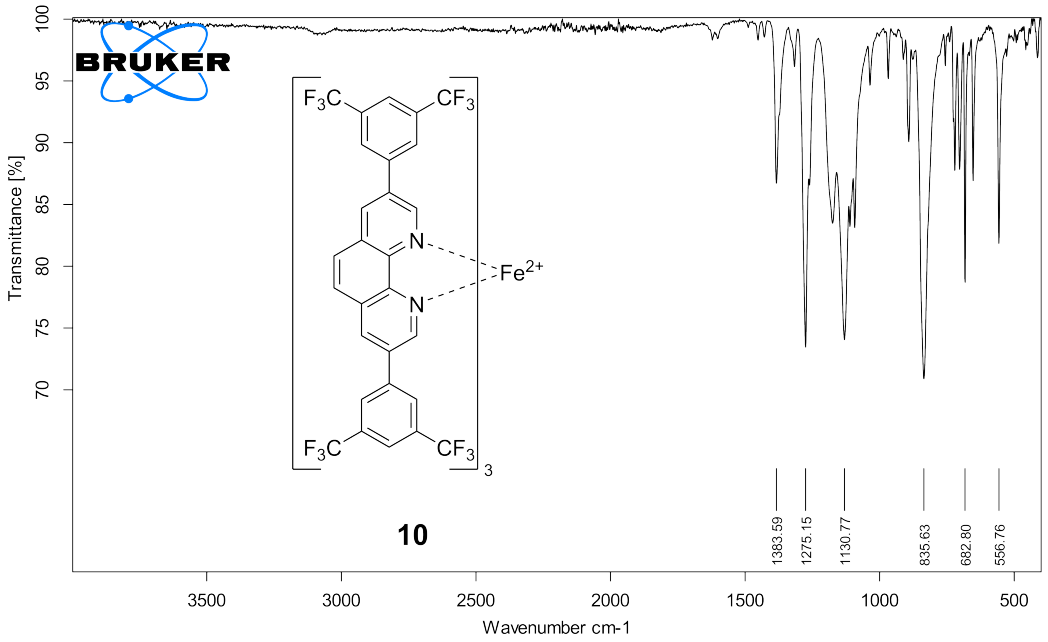

Figure S31: IR spectrum of complex **10**.

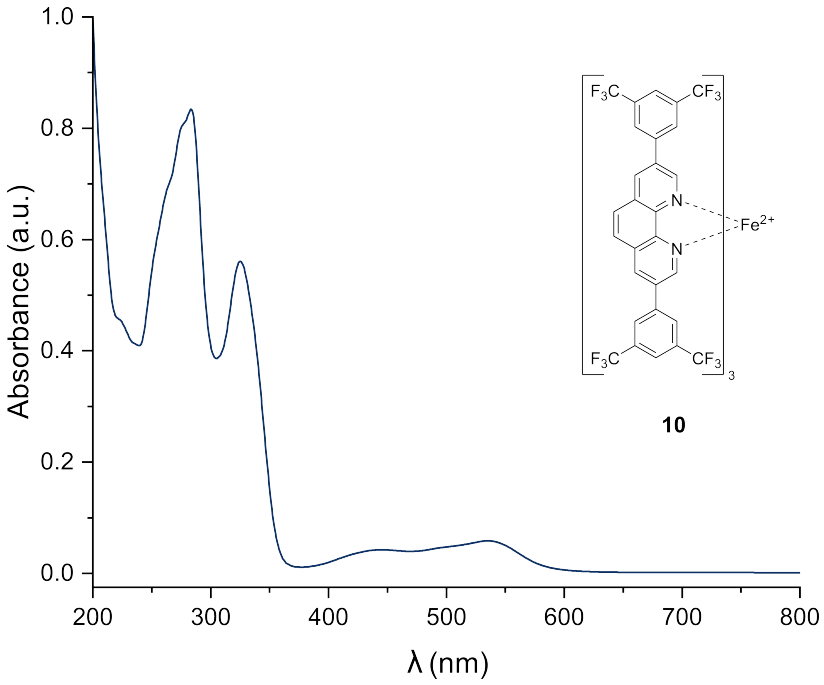

Figure S32: UV/vis spectrum of complex **10** in CH_3CN (0.06 mM).

^{1}H NMR (700 MHz, CD_3CN): δ = 9.09 (d, J = 1.8 Hz, $6H_4$), 8.41 (s, $6H_7$), 8.03 (s, $6H_{11}$), 7.97 (d, J = 1.8 Hz, $6H_6$), 7.91 (s, $12H_9$) ppm.

^{13}C NMR (176 MHz, CD_3CN): δ = 156.29 (C_6), 150.43 (C_2), 138.70 (C_8), 137.10 (C_4), 136.60 (C_5), 132.85 (q, J = 34 Hz, C_{10}), 131.89 (C_3), 130.04 (C_7), 129.20 (m, C_9), 124.18 (q, J = 273 Hz, C_{12}), 123.96 (m, C_{11}) ppm.

^{19}F NMR (659 MHz, CD_3CN): δ = -63.50 (s, $36F_{12}$), -72.98 (d, J = 706 Hz, $12F_{PF_6^-}$) ppm.

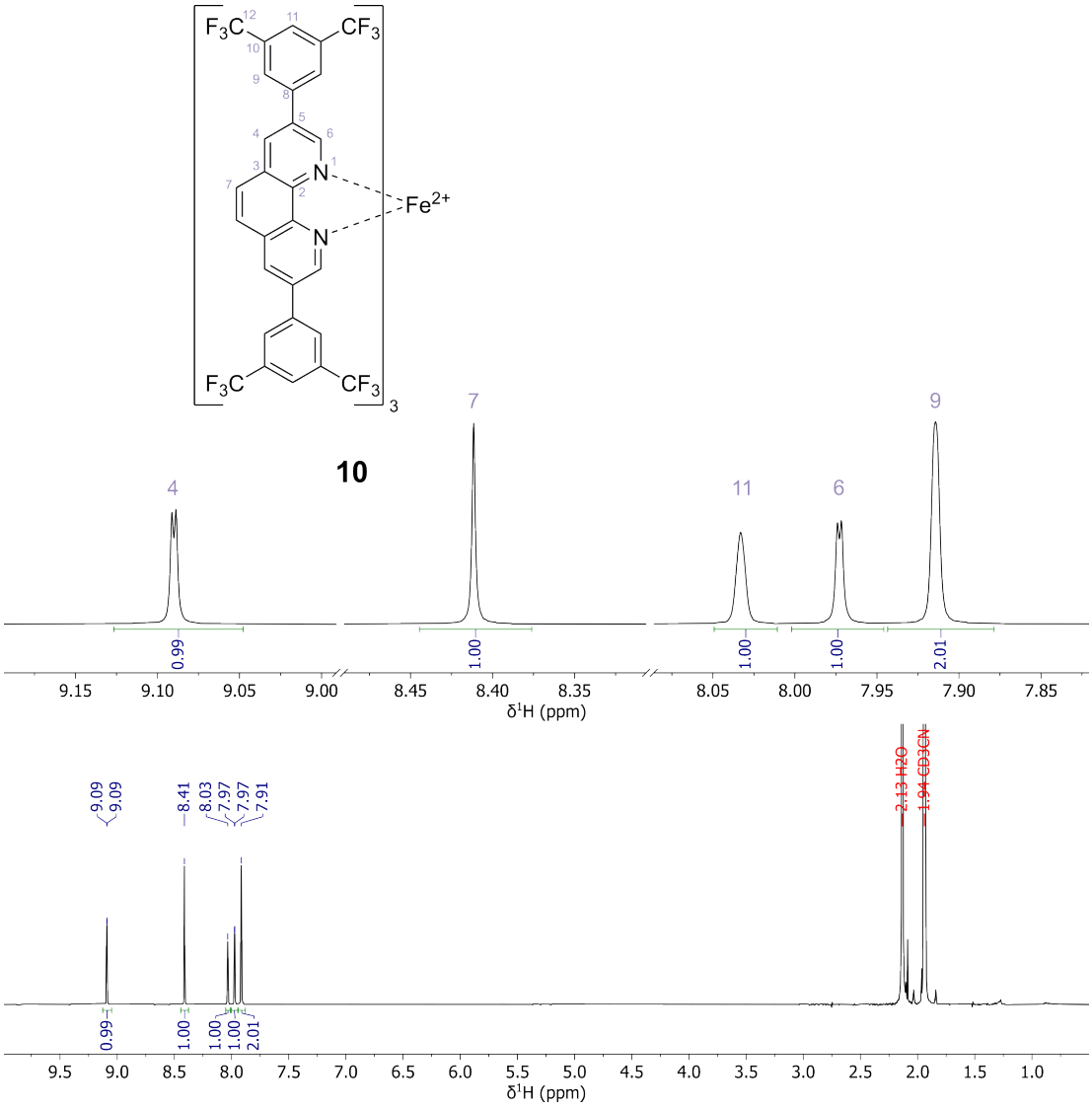

Figure S33: ^{1}H NMR spectrum of complex **10** in CD_3CN at 300 K.

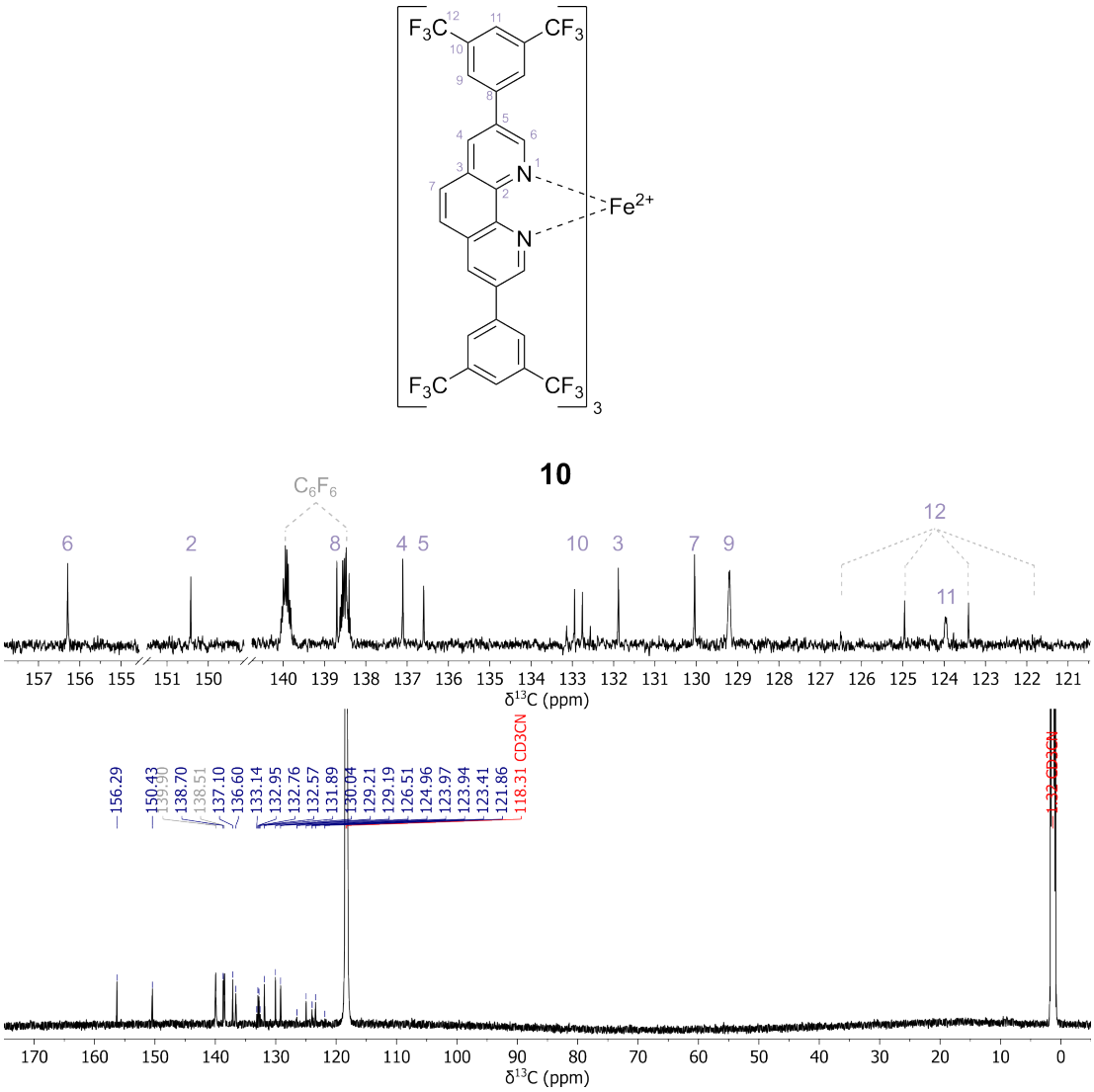

10

Figure S34: ^{13}C NMR spectrum of complex **10** in CD_3CN at 300 K.

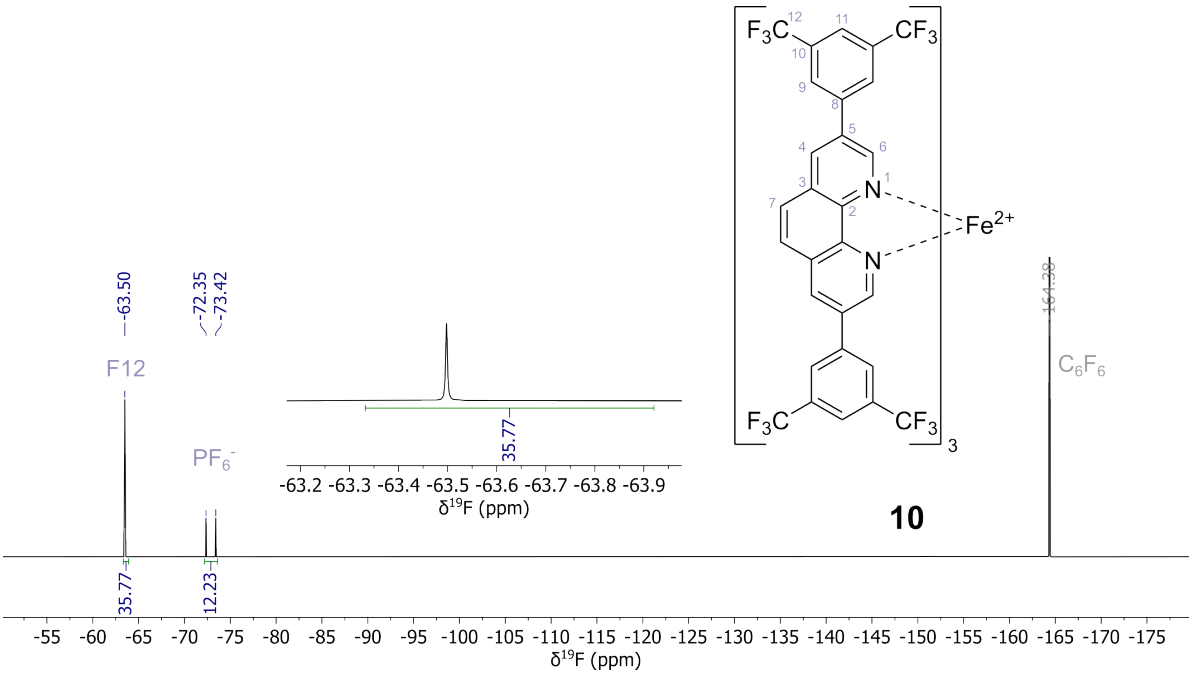

Figure S35: ^{19}F NMR spectrum of complex **10** in CD_3CN at 300 K.

MS (HR-ESI, m/z): $[M]^{2+}$ calculated for $C_{84}H_{36}F_{36}FeN_6$ 934.08825; found 934.08918 (Δ = 1.00 ppm).

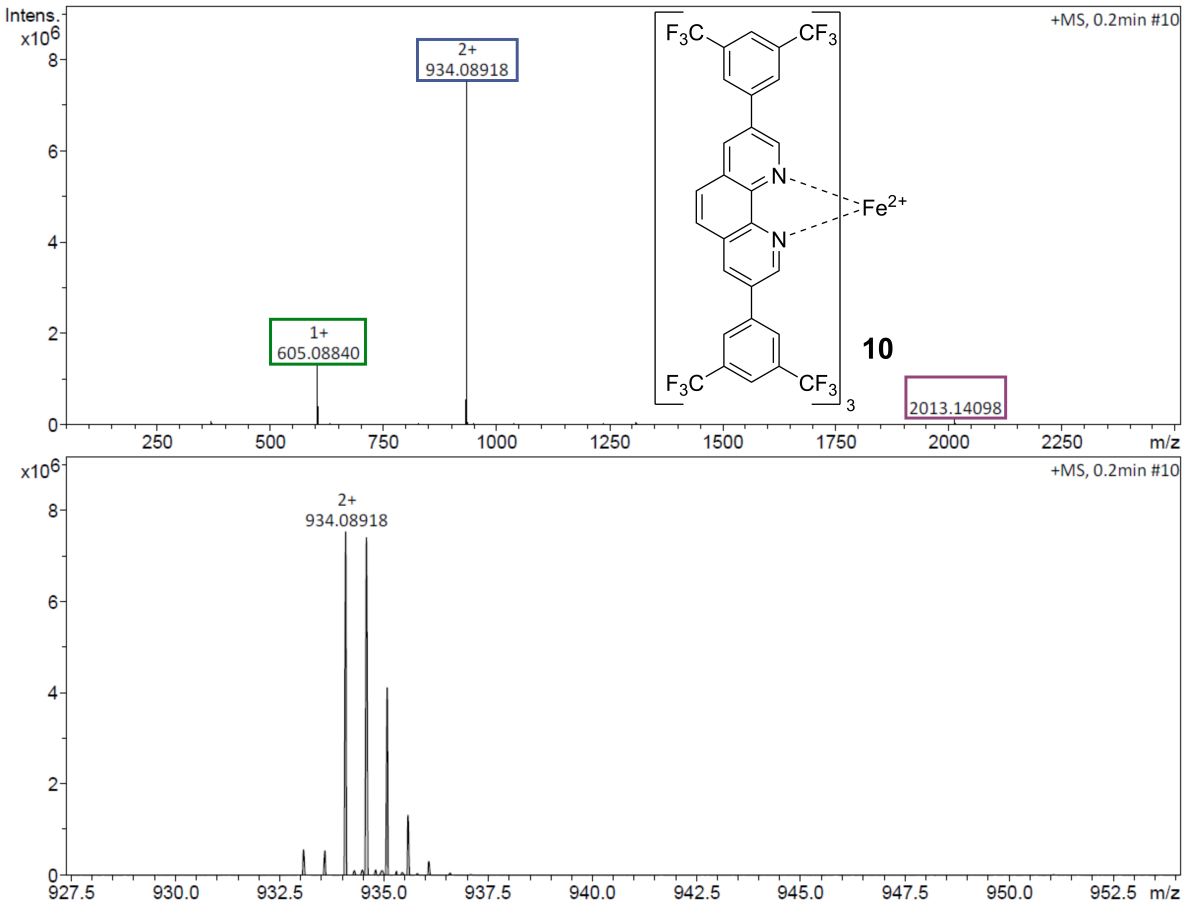

Figure S36: High-resolution mass spectrum of complex **10** acquired as ESI in positive ionisation mode. The double positive charged complex cation is marked in blue, the complex cation with one PF_6^- anion in magenta and the ligand $[H^+]$ in green.

6 CREST

Using the Conformer-Rotamer Ensemble Sampling Tool (CREST) based on the iMTD-GC algorithm,[2] an ensemble of 500 initial structures was generated for complex **4**. These structures were filtered for duplicates using an in-house Python script, and the resulting unique candidates were further optimized using the DFT settings described in the main text. The resulting pool of local minima was again filtered for duplicates, ultimately yielding the ten unique conformers discussed in the main article.

The relative single-point energies after DFT geometry optimisation and the averaged ^{19}F chemical shifts for the three distinct positions along the perfluoropropyl chains (α, β, and γ) are summarized in Table S6.

Table S6: Overview of relative energies and ^{19} chemical shifts for the geometry-optimised structure and the nine unique conformers of $[Fe^{II}(py)_2(por-C_3F_7)_4]$ (**4**) obtained from CREST conformer sampling. Listed are the final single-point energies from the subsequent DFT geometry optimisations (in kcal/mol) and the averaged ^{19}F chemical shifts (in ppm) for F_α, F_β, and F_γ of each conformer using LH20t, the pcSseg-2 basis sets and no relativistic correction.

	FSPE	^{19}F Shifts		
Conformer	[kcal/mol]	F_α	F_β	F_γ
G-OPT	1.23	-91.26	-118.21	-78.59
1	0.00	-84.70	-116.25	-78.37
61	0.22	-82.44	-115.21	-78.10
101	3.10	-83.16	-116.78	-77.52
108	3.07	-96.72	-119.54	-78.53
111	2.47	-97.86	-120.33	-78.83
115	2.74	-98.75	-120.59	-78.79
134	2.88	-96.29	-119.74	-78.43
206	1.18	-81.12	-117.23	-78.63
340	3.01	-84.09	-117.15	-77.68
Exp.		-86.21	-119.37	-79.97

As discussed in the main text, all nine conformers, including the original geometry-optimised structure, are found within an energy window of only 3.1 kcal/mol. Interestingly, the CREST sampling identifies a conformer that lies 1.23 kcal/mol lower in energy than

the initially assigned global minimum. However, when single-point energies are reevaluated using different exchange–correlation functionals, the energetic ordering changes, indicating that these energy differences are within the intrinsic error margin of the underlying DFT method. Therefore, while the exact ranking should not be overinterpreted, it is clear that a variety of conformers are thermally accessible at room temperature.

As illustrated in Figure 6 of the main text, the conformers do not differ significantly in terms of the porphyrin ring bending or the relative orientations of the axial pyridine ligands. Instead, the main structural variations arise from the orientations of the four perfluoropropyl side chains. The side chains can be broadly classified as either in-plane (IP) with respect to the porphyrin macrocycle or out-of-plane (OOP), where the latter category includes chains pointing towards the axial pyridine ligands or folded along the porphyrin edge.

Using this classification, the nine unique conformers can be grouped into three distinct categories:

- Group I: 4 conformers with 1× IP and 3× OOP side chains
- Group II: 3 conformers with 2× IP and 2× OOP side chains
- Group III: 2 conformers with 3× IP and 1× OOP side chain

Notably, none of the sampled conformers feature either 4× IP or 4× OOP side chains, suggesting that such extreme orientations are energetically disfavored.

References

(1) de Oliveira, M. T.; Alves, J. M.; Braga, A. A.; Wilson, D. J.; Barboza, C. A. Do double-hybrid exchange–correlation functionals provide accurate chemical shifts? A benchmark assessment for proton NMR. *J. Chem. Theory Comput.* **2021**, *17*, 6876–6885.

(2) Pracht, P.; Bohle, F.; Grimme, S. Automated exploration of the low-energy chemical

space with fast quantum chemical methods. *Phys. Chem. Chem. Phys.* **2020**, *22*, 7169–7192.

(3) Qu, F.; Nguyen, T. Q.; Janzen, A. F. 4-Fluoro-2, 2-bipyridine (fbpy) complexes of cobalt (II/III) and iron (II/III) and electron transfer in the Co (bpy) 32+–Co (fbpy) 33+ system. *J. Fluor. Chem.* **1999**, *94*, 15–26.

(4) Moore, K. T.; Fletcher, J. T.; Therien, M. J. Syntheses, NMR and EPR Spectroscopy, Electrochemical Properties, and Structural Studies of [5, 10, 15, 20-Tetrakis (perfluoroalkyl) porphinato] iron (II) and-iron (III) Complexes. *J. Am. Chem. Soc.* **1999**, *121*, 5196–5209.

(5) Nößler, M.; Jäger, R.; Hunger, D.; Reimann, M.; Bens, T.; Neuman, N. I.; Singha Hazari, A.; Kaupp, M.; van Slageren, J.; Sarkar, B. Electrochemistry and Spin-Crossover Behavior of Fluorinated Terpyridine-Based Co (II) and Fe (II) Complexes. *Eur. J. Inorg. Chem.* **2023**, *26*, e202300091.

(6) Song, B.-H.; Yu, B.-s. Fluorine-19 NMR spectroscopic studies of phenyl-fluorinated iron tetraarylporphyrin complexes. *Bull. Korean Chem. Soc.* **2003**, *24*, 981–985.

(7) Novotny, J.; Komorovsky, S.; Marek, R. Paramagnetic Effects in NMR Spectroscopy of Transition-Metal Complexes: Principles and Chemical Concepts. *Acc. Chem. Res.* **2024**, *57*, 1467–1477.

(8) Fulmer, G. R.; Miller, A. J.; Sherden, N. H.; Gottlieb, H. E.; Nudelman, A.; Stoltz, B. M.; Bercaw, J. E.; Goldberg, K. I. NMR chemical shifts of trace impurities: common laboratory solvents, organics, and gases in deuterated solvents relevant to the organometallic chemist. *Organometallics* **2010**, *29*, 2176–2179.

(9) Rosenau, C. P.; Jelier, B. J.; Gossert, A. D.; Togni, A. Exposing the Origins of Irreproducibility in Fluorine NMR Spectroscopy. *Angew. Chem. Int. Ed.* **2018**, *57*, 9528–9533.

(10) Gottlieb, H. E.; Kotlyar, V.; Nudelman, A. NMR Chemical Shifts of Common Laboratory Solvents as Trace Impurities. *J. Org. Chem.* **1997**, *62*, 7512–7515.